UNIVERSITATEA “BABEŞ-BOLYAI” CLUJ-NAPOCA

FACULTATEA DE FIZICĂ

SPECIALIZAREA FIZICĂ

LUCRARE DE LICENŢĂ

Coordonator științific

CS I Dr. Botiz Ioan

Absolvent

Cotoarbă Yenda

[2025]

UNIVERSITATEA “BABEŞ-BOLYAI” CLUJ-NAPOCA

FACULTATEA DE FIZICĂ

SPECIALIZAREA FIZICĂ

LUCRARE DE LICENŢĂ

Crystals of non-fullerene acceptors generated by rich exposure to solvent vapors

Coordonator științific

CS I Dr. Botiz Ioan

Absolvent

Cotoarbă Yenda

[2025]

Acknowledgements

In this section I want to take a moment to express my deepest gratitude and appreciation to my supervisor, CS I dr. Botiz Ioan, for his patience, insight and support throughout this journey. His aspiration for excellence, attention to detail and lightheartedness made this study enjoyable. My appreciation also goes to dr. Otto Todor-Boer for taking the time to help us in this quest. Additionally, I want to thank the Institute for Interdisciplinary Research in Bio-Nano-Sciences for putting their infrastructure and resources at my disposal. Finally, I must also express my unlimited appreciation for my family, without whose support and sacrifices I would not have been here.

Abstract

Non-fullerene acceptors play a significant role in the fabrication of high-efficiency energy conversion devices. Their performance, particularly their optoelectronic properties, is highly dependent on the precise molecular arrangement at both the microscale and nanoscale levels. Having the ability to precisely control these structures is crucial for improving device functionality. In the present work, we report an advancement, by successfully fabricating the first highly ordered (single) crystals of Y6 and Y12. This resulted from carefully controlling the exposure of these non-fullerene acceptors to generous amounts of solvent vapors. The fabricated crystals displayed a considerable diversity in shape, size, density and long-range morphology, all depending on the type of solvent used and the employed evaporation rate. The most important detail about the obtained Y6 and Y12 crystals is that they displayed unexpected and potentially valuable absorbance properties, suggesting a further need for investigation for future applications. Furthermore, the experimental results highlight the close relationship between microstructure, processing and the resulting properties. A deeper understanding of these materials could potentially lead to significant advancements in the development of new and enhanced energy devices.

NOTE: Parts of the abstract were utilized or adapted from the article that was previously published by us: [1]

Table of Contents

Introduction

Non-fullerene acceptors (NFAs) are mainly known for their applications in the domain of organic solar cells. Their suggestive name distinguishes them from the fullerene acceptor molecules category, that previously dominated bulk heterojunction organic solar cell research and development. The transition to these types of compounds started because fullerene acceptors have a high electron mobility and can be easily paired with polymer donors. This resulted in a cost-effective and high-performance alternative to the existing energy sources present. However, the precise tuning of energy levels in these devices proved to be quite challenging and the absorption properties were suboptimal. Thus, the rise of non-fullerene acceptors came into being. These materials could overcome the obstacles that were met for fullerene acceptors, especially in the form of small molecules, with the main disadvantage being their morphological disorganization which was aimed at being improved in this study.

Y6 and Y12 are two NFAs, specifically designed for applications in organic electronic devices, the main difference between them being an increase in solubility for the latter. Both possess an electron-deficient core and a fused ring structure, featuring great utility in the field of organic photovoltaics. In order to fully optimize the performance of Y6 and Y12, it is essential to design and develop sophisticated processing methods capable of rigorously controlling and tuning their molecular arrangements at macro-, micro- and nanometer scales. As such, achieving surface improvements in the field of optoelectronics can be possible only by understanding the intricate relationship between microstructure, processing and resulting properties.

There exists a great variety of thin film coating methods which are extensively documented in the literature including techniques such as spin-, dip-, roll-, spray- or blade-coating. However, in this study, the main focus was on the fabrication Y6 and Y12 films using spin-coating and convective self-assembly, with the latter being a member of the blade-coating family. After removing a piece of every film which served as a reference, the remaining pieces underwent a processing post-treatment such as, confined solvent vapor annealing or thermal annealing. The first method mainly involves exposing the films to controlled amounts of solvent vapors, transforming solid films into “film-solutions” and allowing the formation of crystalline structures on the surfaces, followed by increasing the temperature until the films are thoroughly dried again. The second method, on the other hand, entails heating the films above their melting temperatures and observing whether the morphology became more ordered as a result. These methods were used because of their recognized ability of inducing self-assembly and promoting crystallization. Furthermore, the altered morphologies of the obtained films were closely observed through optical

microscopy, atomic force microscopy and UV-vis spectroscopy. As was revealed by these investigation methods, Y6 and Y12 crystals have been obtained. The crystals vary in shape, size and density depending on the solvent type used and the evaporation rate.

Perhaps the most intriguing observation is that the absorption properties were successfully modified when compared to the reference spin-cast films, attributed to an increase in molecular ordering. It is important to emphasize that these results could not be replicated using any other processing method employed in this work. This further highlights the challenge of obtaining these crystals and the important consequences on the morphological order of films by exposing them to confined solvent vapor annealing.

Chapter 1

Fullerene and non-fullerene materials as acceptors in organic solar cells

1.1 A brief overview of organic solar cells

The demand for energy keeps increasing on a daily basis leading to the depletion of available resources and global changes, this is especially caused by the consumption of non-renewable energy, thus the search for renewable energy started years ago and it seems that a less toxic and better alternative, not just to the more harmful sources, but also to inorganic solar cells has been found, namely organic solar cells (OSCs). Several other reasons such as low cost, lightweight, flexibility and the possibility to undergo solution processing [2], [3], [4] have attracted a lot of attention towards them.

OSCs usually consist of at least 4 layers, without counting the substrate on which the cathode is placed, followed by the active layer, between which one can usually find a layer of a conductive mixture with the purpose of helping with transportation of holes, blocking oxygen from the active layer and making the cathode-active layer diffusion impossible. Finally, lies the anode underneath which a protective layer of lithium fluoride is placed.

The core mechanism for every type of OSC is the same, namely the absorption of photons by the active layer creates excitons (electron-hole pairs that are bound by a strong coulombian attraction), which dissociate, creating electrons and holes. In heterojunction devices this dissociation only contributes to generating current if the diffusion reaches the donor/acceptor (D/A) interface, if not the exciton relaxes back to the ground state. The lowest unoccupied molecular orbital (LUMO) and highest occupied molecular orbital (HOMO) energies of the donor material need to be higher than the energies of the acceptor to be able to reach the acceptor and donor phase. Resulting in the movement of the electrons and holes along the acceptor and donor network, under the influence of the inner electric field.

Heterojunction implies that the active layer consists of 2 materials, donor and acceptor, which are responsible for the charge carrier diffusion and generating, respectively dissociating excitons. Thus, controlling the structure of the active layer plays a crucial role in the design of solar cells. The most used architectures for this layer are bulk and bilayer heterojunction, but each one comes with its own limitations [5], [6].

Bulk heterojunction (BHJ) relies on blending the donor and acceptor of the active layer in a way to enhance the interface between their phases. Even though this method of enhancing the nanoscale morphology is very researched, illumination and thermal aging tend to limit its lifetime, resulting in a gradual segmentation of the D/A areas. [7]

The layer-by-layer (LBL), or bilayer architecture removes itself from the unstable blends seen in BHJ, by adopting donor and acceptor materials with an orderly, planar junction, which can be treated separately leading to a higher morphological stability. [8]

Therefore, to optimize OSCs (or even other devices such as organic field-effect transistors/OFETS or light-emitting diodes/OLEDs), it is useful first to optimize the microstructure and correspondent optoelectronic properties of the two components both in blend and neat active films. In this work we will focus our studies only on neat films made of the electron accepting component.

1.2 Non-fullerene acceptors

As mentioned above, all systems include active layers which partly consist of organic electron acceptors such as small molecules [9], [10] and donor materials, which are usually conjugated polymers [11], [12]. The most widely used small molecules used to be fullerenes, because of their high electron affinity, but the results were disappointing due to the poor absorption of light [10], limited stability [13] and restricted capacity for adjusting energy levels [14]. Thus, the focus of researchers shifted towards non-fullerene acceptors (NFAs), which in demonstrations outperformed fullerenes [15], exhibiting broader light absorption spectra [16] and good intramolecular charge transfer [17], leading to actual promising results in what concerns OSCs with PCEs as high as 20% [18]. Aside from this, the progress of LBL heterojunction OPVs started with the NFA movement, up until then fullerenes slowed this progress down because of their reduced diffusion length [19].

Fused ring electron accepting small molecules are a subgroup of NFAs, which as the name suggests, contain multiple aromatic rings that are fused together, forming a “ladder-type” structure. The central unit is a strong electron donating fused ring, with two strong electron accepting endgroups attached to it.

Some other important factors which have led to a growing interest in fused-ring electron accepting small molecules are their well-defined molecular-weights and an easier purification in contrast to large macromolecules [20], [21]. Over the years many different NFAs have been studied such as ITIC [22], IDIC [23], INPIC [17], their derivatives [24], [25], [26], [27], but a lot of attention nowadays is centered on Y6 [28] and its families, especially one derivative known as

Y12, because of their great power conversion capabilities. As a result, by studying and improving these types of materials charge transport properties can be optimized.

The main advantage of Y6 is that it can absorb light in the complete visible and near infra-red spectrum. Multiple studies have shown that in combination with wide-bandgap donor polymers OSCs with PCEs of 15-16% [28], [29], [30] can be obtained. Whereas the main difference between Y6 and Y12, is that the latter is more soluble, leading to better solution processability when blended with low-bandgap donor polymers, resulting in PCEs as high as 17.4% [31], [32].

1.3 Theoretical perspective and experimental approach

The optoelectronic properties of devices need to be optimized for better organic devices. To do so, an understanding of the physical processes resulting from controlling the structures of materials with appropriate techniques and at appropriate scales is crucial and can result in major breakthroughs in the world of material science.

There exists a great variation in processing procedures which one can read about in the existing literature but briefly put the most used techniques rely on the physical process of either self-assembly, or crystallization. This is realized through solvent vapor annealing, thermal and melt annealing, as well as confinement of space which are part of post-treatments, whereas a lot of studies also rely on finding a great balance and combination between the chosen materials by altering their structures through side chain engineering, using different fused rings, etc. [9], [33], [34], [35], [36], [37].

Thermal annealing (TA) is a post-treatment which consists of heating the studied material above the glass transition temperature, and eventually the melting temperature, for a certain amount of time, which allows structural modifications such as recovery from deformations, recrystallization (creation of new and improved crystals) or phase transformation. The heating is followed by a certain cooling process such as full annealing, process annealing or quenching. For solvent vapor annealing (SVA) the studied film is placed in a specific solvent vapor, which provokes an orderly reassembly of the morphological structure.

Y6 and Y12, which have been proven to be great NFAs, due to their fused-ring, ladder-type structure, can be further improved by understanding the close relation between processing methods and their effects on the microstructure and properties of materials. For example, a high level of crystallinity can be advantageous for charge transfer, and this is exactly what we aimed to generate in this work by employing a procedure that was previously developed to self-assemble [38] and crystallize [39] various copolymers [40] and biopolymers [41], known as solvent vapor annealing in a quasi-confined environment (C-SVA). The reproduction of the phenomenon known

as rich swelling of thin films in solvent vapors, is brought to life with a homemade setup, which turned solid state Y6 and Y12 films into "film-solutions", through condensing generous amounts of solvent vapors extracted each second during the process of film deswelling.

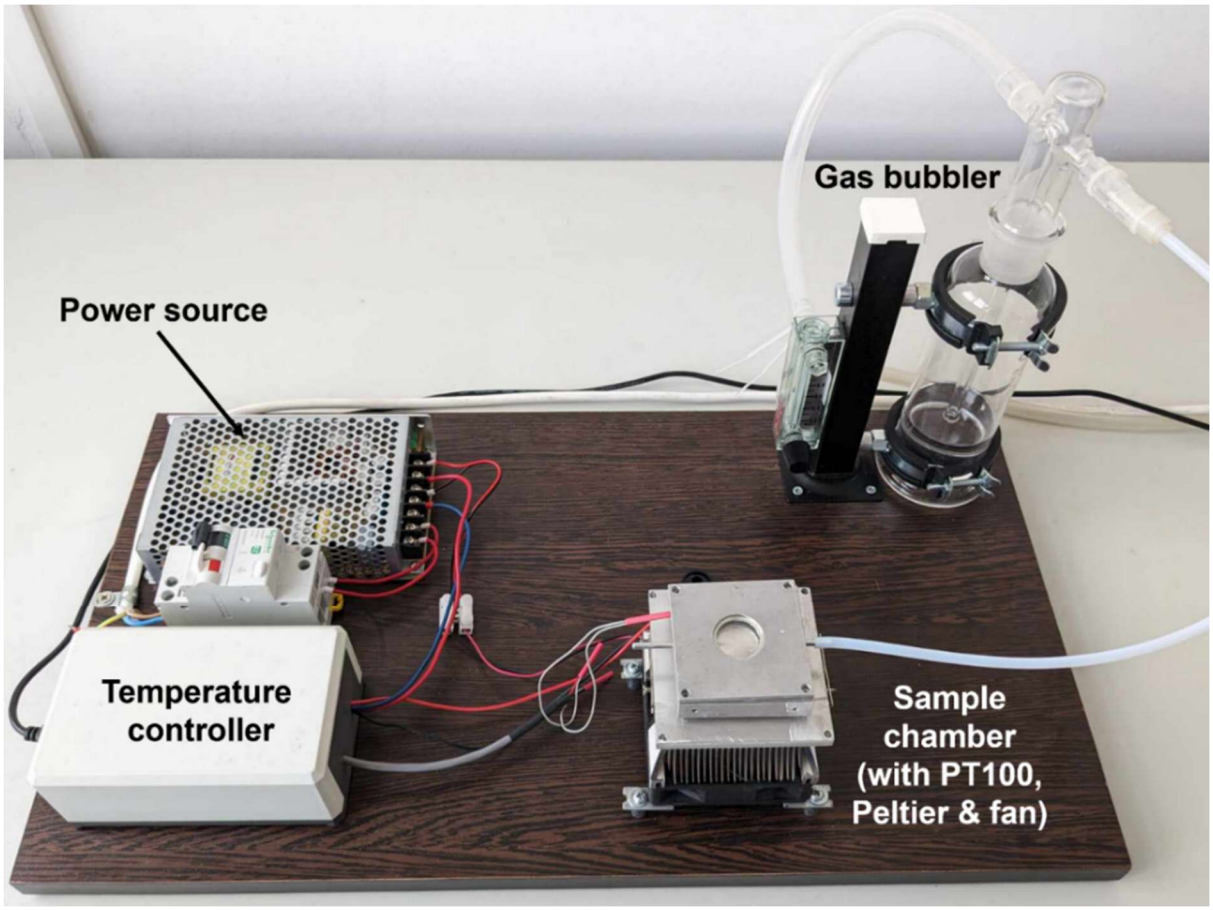

Figure 1.1 Digital photograph of the homemade setup, consisting of a aluminum sample chamber, connected to a high-performance Peltier element, a PT100 temperature sensor and a fan, temperature controller (connected to a software), power source and gas bubbler (allows introduction of controlled amounts of vapors). This figure was reproduced with permission from ref. [1].

The experimental C-SVA configuration is comprised of an aluminum chamber (of reduced depth) covered by a glass window, which offers the confinement suggested by the name of this technique. The chamber is connected to a high-performance Peltier element (15.4 V/8.5 A from Stonecold), regulated by a controller (TCM U 10A from Electron Dynamics Ltd., Southampton, UK), a PT100 temperature sensor (located near the film) and a fan (for heat evacuation). The entire setup is connected to a software, which allows controlling the temperature with a rate as precise as 0.01 ºC/s. The adjacent bubbling system allows injection of precise quantities of solvent vapors (chlorobenzene and chloroform in this study). The thin Y6 and Y12 films are inserted into the sample chamber, followed by the injection of solvent vapors, turning the solid films into "film-

solutions" by lowering the temperature and forcing a condensation onto the samples. Reassembly or crystallization can be closely supervised by controlling the extraction rate of the solvent vapors per second, when increasing the temperature in the deswelling phase.

NOTE: Parts of this chapter were either utilized or adapted from the article that was previously published by us: [1]

Chapter 2

Materials and Methods

2.1 Studied non-fullerene acceptors

Y6, also known as BTP-4F, stands for 2,2'-((2Z,2'Z)-((12,13-bis(2-ethylhexyl)-3,9-diundecyl 12,13-dihydro-[1,2,5]thiadiazolo[3,4-e]thieno[2",3'':4',5']thieno[2',3':4,5]pyrrolo[3,2-g]thieno [2',3':4,5]thieno[3,2-b]indole-2,10-diyl)bis(methanylylidene))bis(5,6-difluoro-3-oxo-2,3-dihydro -1H-indene-2,1-diylidene))dimalononitrile. Whereas Y12, also known as BTP-4F-12, stands for 2,2'-((2Z,2'Z)-((12,13-bis(2-butyloctyl)-3,9-diundecyl-12,13-dihydro-[1,2,5] thiadiazolo[3,4-e] thieno[2",3":4',5']thieno[2',3':4,5]pyrrolo[3,2-g]thieno[2',3':4,5]thieno[3,2-b] indole-2,10-diyl)bis (methanylylidene))bis(5,6-difluoro-3-oxo-2,3-dihydro-1H-indene-2,1-diylidene))dimalononitrile. Their chemical structures ca be seen in Figure 2.1.a and 2.1.b, respectively.

Y6 and Y12 are A-DA'D-A type NFAs, with molecular weights of 1451.93 g/mol and 1564.18 g/mol, respectively. Both NFAs have been purchased from Ossila Ltd. (Sheffield, UK).

The underlying main component is a ladder type electron-deficient central benzothiadiazole (BT) based core unit which helps with charge separation and transportation due to its low bandgap and heightened electron affinity. The electron rich backbone consisting of a fused thiophene ring mainly influences the LUMO and enhances charge carrier mobility. The electron deficient end groups, in which fluorine can be found, interact with sulfur and hydrogen, forming non-covalent bonds. In other words, more intermolecular interactions appear, leading to better optical absorption. The side chains are alkyl groups mainly increase solubility and decide on the spatial arrangement, whereas the electron-withdrawing bulky groups reduce the loss of voltage in solar cells. The HOMO level increases because of the bridging nitrogen atoms, which possess a strong electron donating character and implicitly optimize charge carrier mobility. Finally, the pi-conjugated backbone can be controlled by the pi spacers.

The only difference between Y6 and Y12 is that the latter has two butyloctyl side chains, as opposed to the two ethylhexyl chains seen in the first mentioned component. This modification enhances solubility, meaning that solution processability can be better applied [42], [43], [44], [45].

2.2 Fabrication and processing methods

The reagent used for creating solutions was chloroform (98.5%), acquired from Chemical Company (Iasi, Romania). Two solutions (8 mg/mL) were obtained by dissolving 16 mg of Y6, respectively Y12, in 2 mL of $CHCl_3$, followed by stirring for 30 minutes at room temperature.

2.2.1 Spin casting of thin films

Thin films of Y6 and Y12 (119±8 nm in thickness) were obtained by spin casting the $CHCl_3$:Y6 and $CHCl_3$:Y12 solutions onto UV-ozone cleaned glass coverslips or silicon wafers (type 4P0/5–10/380 ± 15/SSP/TTV<5 from Siegert Wafer) utilizing a WS-650mz23nppb spin-coater from Laurell Technologies Corporation (North Wales, PA, USA) at 2000 rpm for 30 s.

2.2.2 C-SVA post-treatment on thin films

By inserting the Y6 and Y12 films consecutively into the sample chamber of the aforementioned homemade C-SVA setup, the swelling and deswelling process was stimulated through injection of solvent vapors.

After putting a NFA film into the covered chamber, the enclosed space was soaked with a precisely adjusted quantity of solvent vapors and heated to 40° C. Afterwards, the film temperature was lowered at a rate of 0.3° C/s until reaching around 15-20° C (for example, 15° C was used for more volatile chlorobenzene and less soluble Y6). In this temperature interval, the most prominent solvent condensation could be seen on the films, through the change of interference colors, visible to the naked eye or under an optical microscope, especially when using silicon wafers. The exact temperature depends on the used solvent, its volatility and of course the chosen NFA.

As one can see in Figure 2.1.c, in the condensation phase the thickness of the film suffers a dramatic increase, known as the swelling process. Here the films suffer a transformation from their solid state into quasi 2D film-solutions. This process was followed by the deswelling phase, which has been initiated by heating, or in other words annealing, the films at different rates, namely at 0.25° C/s, 0.07° C/s, 0.01° C/s. In the time in which the solvent was extracted, nucleation and crystallization was stimulated. By the time that the initial temperature of 40° C was reached again through heating, the films were completely dry, regaining their initial thickness but having a fundamentally altered morphology. (further details about the process, method and setup can be found in reference [46])

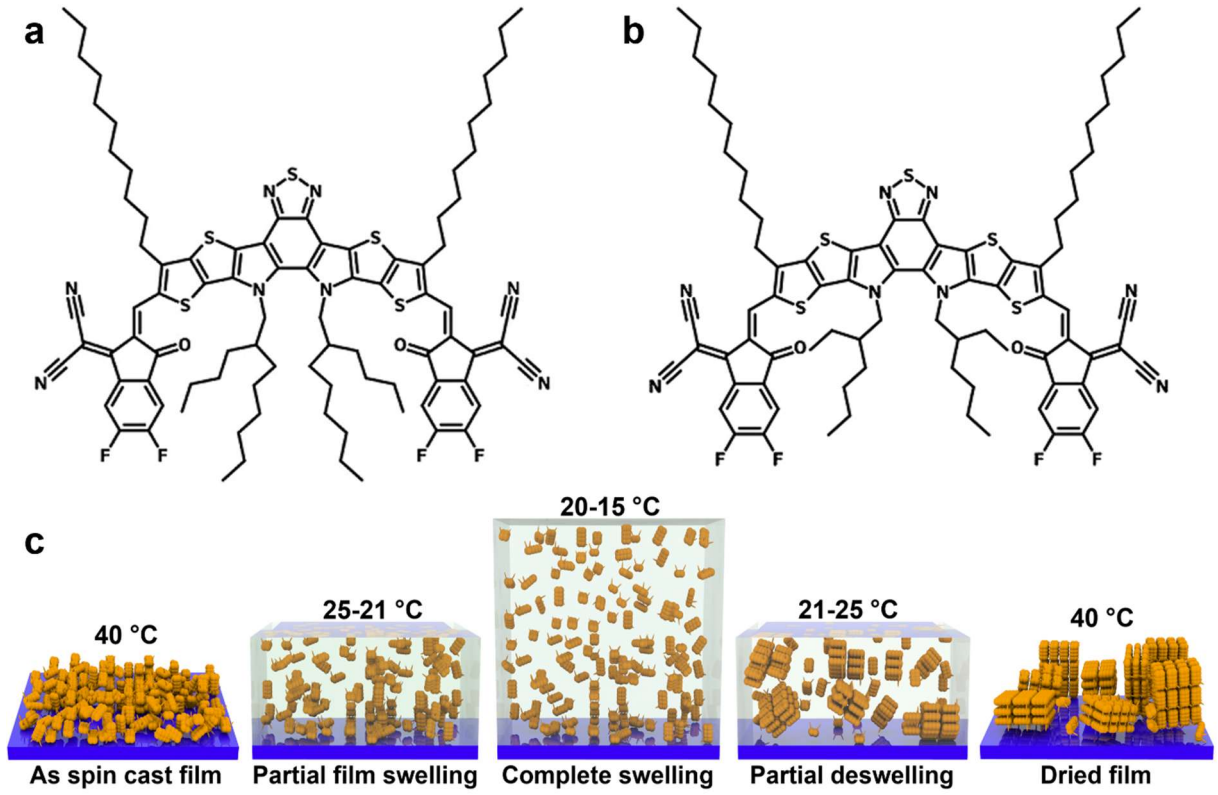

Figure 2.1 (a-b) Chemical structures of Y12 (a) and Y6 (b) NFAs. (c) Illustration of film swelling and deswelling.

2.2.3 Thermal annealing

Some Y6 and Y12 films underwent thermal annealing, right after spin casting. This procedure was executed at high temperatures by employing a hot stage (model THMS 600 from Linkam Scientific), which can control temperature in a broad range, namely between -195° C and 600° C.

2.2.4 Convective self-assembly of thin films

Instead of spin casting, some Y6 and Y12 films were obtained by using convective self-assembly (CSA). This was possible by using a homemade setup which consists of a linear actuator from Zaber Technologies which assembles a motorized translation stage. On top of this there is a temperature controller which has not been used for this experiment, so it was merely left at room temperature. By setting the wanted angle for a cover glass which acts like a blade, the Y6 and Y12-based solutions were poured near it. The results were thin, homogenous films, created at various deposition speeds: 500 µm/s, 50 µm/s and 10 µm/s (further details about the setup and method are available in reference [47]).

2.3 Material investigation methods

2.3.1 Optical microscopy

A superficial view of the resulted morphology of the films, after undergoing processing methods, was possible by using a KERN OKN-177 Optical Microscope Kern Sohn Gmbh Balingen Germany. The acquisition of photos inserted in this work has been employed by using the reflectivity mode of the optical microscope, which was equipped with magnification objectives and a KERN ODC 825 (5 Mp) camera. This setup was connected to a computer and by using the Microscope VIS software, pictures of the areas which were about to undergo an atomic force microscopy investigation, were taken.

2.3.2 Atomic force microscopy

Atomic force microscopy (AFM) is an investigation method, invented in 1985, which provides information about the surface topology of a wide variety of surfaces such as polymers, biological samples, ceramics etc.

The technique primarily relies on a sharp tip that is raster-scanned across the sample. Atomic forces between the probe and the tip are measured to gather information about their interactions. There are many AFM techniques which are capable of analyzing different types of force interactions, including van der Waals, electric, magnetic or thermal. These forces are typically calculated by measuring the deflection of the cantilever. Aside from this, a laser beam is reflected from the back of the cantilever into a photo detector, which produces images of the surface topography.

Another different property of AFM is its ability to function in two modes: contact and non-contact mode. As the names suggest, in contact mode, the tip is in direct contact with the surface, whereas in non-contact mode, the cantilever oscillates near the surface without actually coming in contact, resulting in surface imaging without physical interaction [48], [49].

The AFM images in this study were recorded in a non-contact mode, also referred to as tapping mode, using a system from Molecular Devices and Tools for Nano Technology (NT-MDT, from Spectrum Instruments Ltd., Limerick, Ireland). High resolution NANOSENSOR probes from NanoAndMore GmbH were used. The radius of the used tip was about 7 mm, with a resonance frequency of 75-265 kHz. The tapping regime can be characterized as a soft tapping regime using a set point of 9-12 V.

2.3.3 Absorption spectroscopy

Absorption spectra of all films were acquired using a V-530 UV-VIS spectrophotometer from Jasco. This spectrophotometer's design permits measurements in the wavelength interval of 190-1100 nm. This device utilizes two different light sources: a deuterium (D2) lamp for the UV region (from 190 to 350 nm), and a halogen (WI) lamp for the VIS/NIR region (from 340 to 1100 nm). The emitted light enters a monochromator, where dispersion takes place because of a grating and it is then directed towards the exit slit. The resulting monochromated light was firstly used to record the spectra of a reference sample, the as spin-cast reference films in our case. This was followed by measuring the absorption of the processed samples. The reflected light is directed onto a silicon photodiode which allows the formation of a spectrum [50].

NOTE: Parts of this chapter were either utilized or adapted from the article that was previously published by us: [1]

Chapter 3

Processing and analysis of Y12 films

3.1 Y12 films fabricated by spin-casting

3.1.1 Optical micrographs and AFM images of films processed via C-SVA

Starting with Y12 in Figure 3.1 one can see the optical micrographs of the spin-cast thin film as a reference in comparison to the films processed via C-SVA in chloroform and chlorobenzene, respectively. The results indicate that, although there was no formation of crystals upon spin-casting – aside from small irregular submicrometric structures as can be seen in Figure 3.1g – numerous Y12 crystals randomly emerged and grew after undergoing C-SVA processing, as can be seen in Figure 3.1a-f. Furthermore, a clear dependence between density or dimension and the solvent evaporation rate is visible, where the latter was controlled by the film annealing rate.

Notably, when using the lowest solvent evaporation rate, specifically during the annealing process conducted at 0.01 ºC/s, the largest and least dense Y12 crystals formed, as illustrated in Figure 3.1a-b. For instance, when chloroform vapors where used and evaporated at a film annealing rate of 0.01 ºC/s, around 2.2×10^{-3} Y12 crystals formed of an average length/width of 29/16 µm per square micrometer. Conversely, when increasing the evaporation rate to 0.25 ºC/s, a significantly larger number of crystals ($24.5\times10^{-3}/\mu m^2$) formed, but their length/width decreased to 6/3.5 µm (see Figure 3.1h).

A similar behavior occurred in Y12 films which were processed via exposure to chlorobenzene vapors (Figure 3.1b,d,f). This pattern, which is further illustrated on a larger scale in Figure 3.2, was not entirely surprising.

The slowest solvent evaporation rate provided optimal conditions for nucleation and growth of crystals, but the lower concentration of Y12 resulted in the formation of only a limited number of crystals, which was expected in this relatively “diluted” environment. In contrast, higher evaporation rates, particularly those at or above 0.07 °C/s, favored the formation of a greater number of crystals, but at higher Y12 concentrations. Under these conditions, the resulting crystals had the tendency to grow less, resulting in their relatively smaller dimension. This can be explained by taking into consideration the intense competition for the limited free Y12 molecules available within the constrained "film-solution" reservoir.

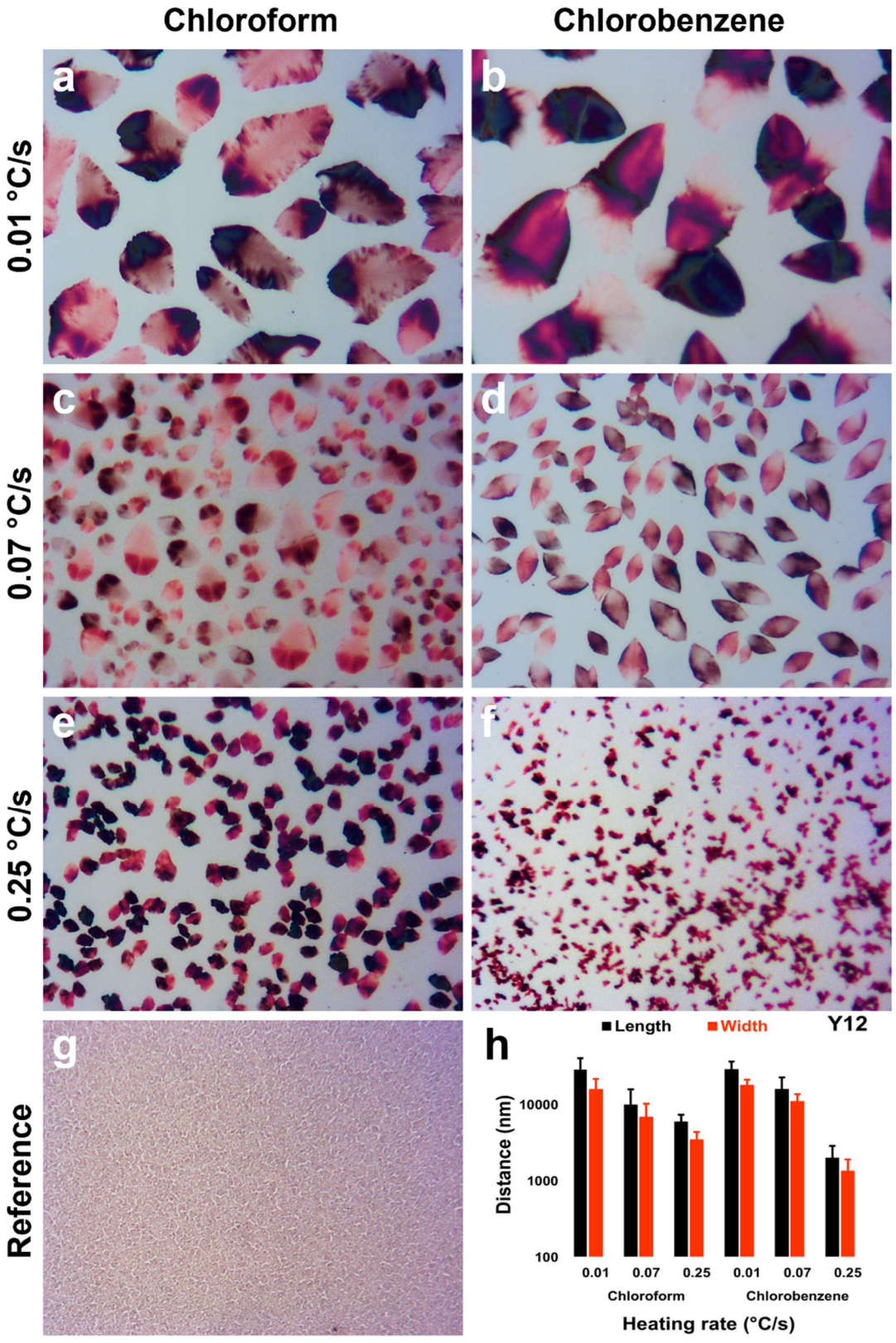

Figure 3.1 (a-f) Optical micrographs of Y12 films exposed to chloroform (a, c, e) and chlorobenzene (b, d, f) vapors. Latter were extracted at a film annealing rate of 0.01 °C/s (a-b), 0.07 °C/s (c-d) and 0.25 °C/s (e-f), respectively. (g) Surface of a reference Y12 film. Size of all micrographs is 120×90 μm^2. (h) Average length and width of Y12 crystals as a function of film annealing rate. Image reproduced with permission from ref. [1].

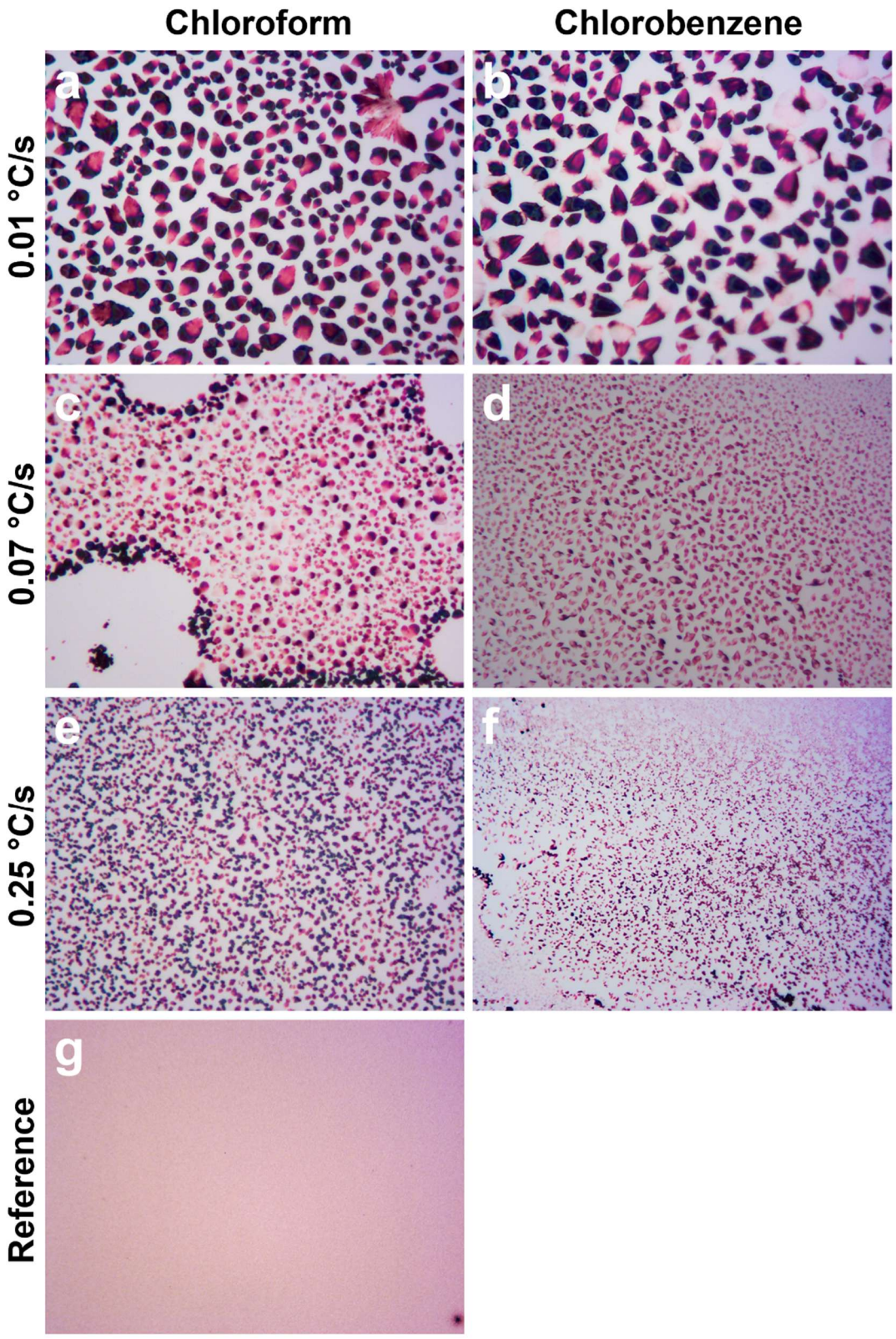

Figure 3.2 Optical micrographs depicting the surface of thin films of Y12 processed via C-SVA in chloroform (a, c, e) and chlorobenzene (b, d, f), while evaporating solvent vapors at a sample annealing rate of: 0.01 °C/s (a-b), 0.07 °C/s (c-d) and 0.25 °C/s (e-f), respectively. The surface of the corresponding spin-cast (*i.e.*, unexposed) Y12 film is shown in (g) for comparison. The size of all micrographs is 480×360 μm^2. Image reproduced with permission from ref. [1].

Further, to gain a deeper understanding of the morphology of Y12 crystals, the AFM technique has been employed. The obtained results are illustrated in Figure 3.3, which reveals that the Y12 crystals are three-dimensional objects with an acorn-like shape characterized by two distinct regions: the “pericarp” and the “cupule”. While the AFM images suggest a long-range order present within each of these two regions, the structure of whole crystals is most likely composed of Y12 molecules that are organized into at least two different types of structural arrangements. These arrangements can be more clearly visualized in Figure 3.4 and they correspond to each respective region of the crystals. A possible cause for these distinct morphological configurations is that they could have developed at two separate growth stages, which were attained throughout the continuous evaporation of solvent vapors.

Larger Y12 crystals formed at lower film annealing rates of 0.01 ºC/s and 0.07 ºC/s. They exhibited a pronounced concave acorn-shaped appearance, as illustrated in the insets of Figure 3.3a-d. In contrast, the less developed crystals which formed under the highest film annealing rate of 0.25 ºC/s, appeared to have a more convex acorn-like shape, as shown in the insets of Figure 3.3e,f. This observation highlights the incomparability of the morphology of the formed crystals compared to the shapeless, irregular structures observed in the Y12 reference film, as depicted in Figure 3.3g.

Furthermore, alongside these morphological differences, we also noted a dependence between the average height of the acorn-shaped crystals as a function of the chloroform evaporation rate. The average height of the crystals decreased with the increase of the evaporation rate, with the measured heights being 160 nm, 110 nm and 85 nm, respectively (Figure 3.3h). A similar trend was observed when exposing the Y12 films to chlorobenzene vapors, strengthening the idea that solvent evaporation rate and crystal morphology are intertwined.

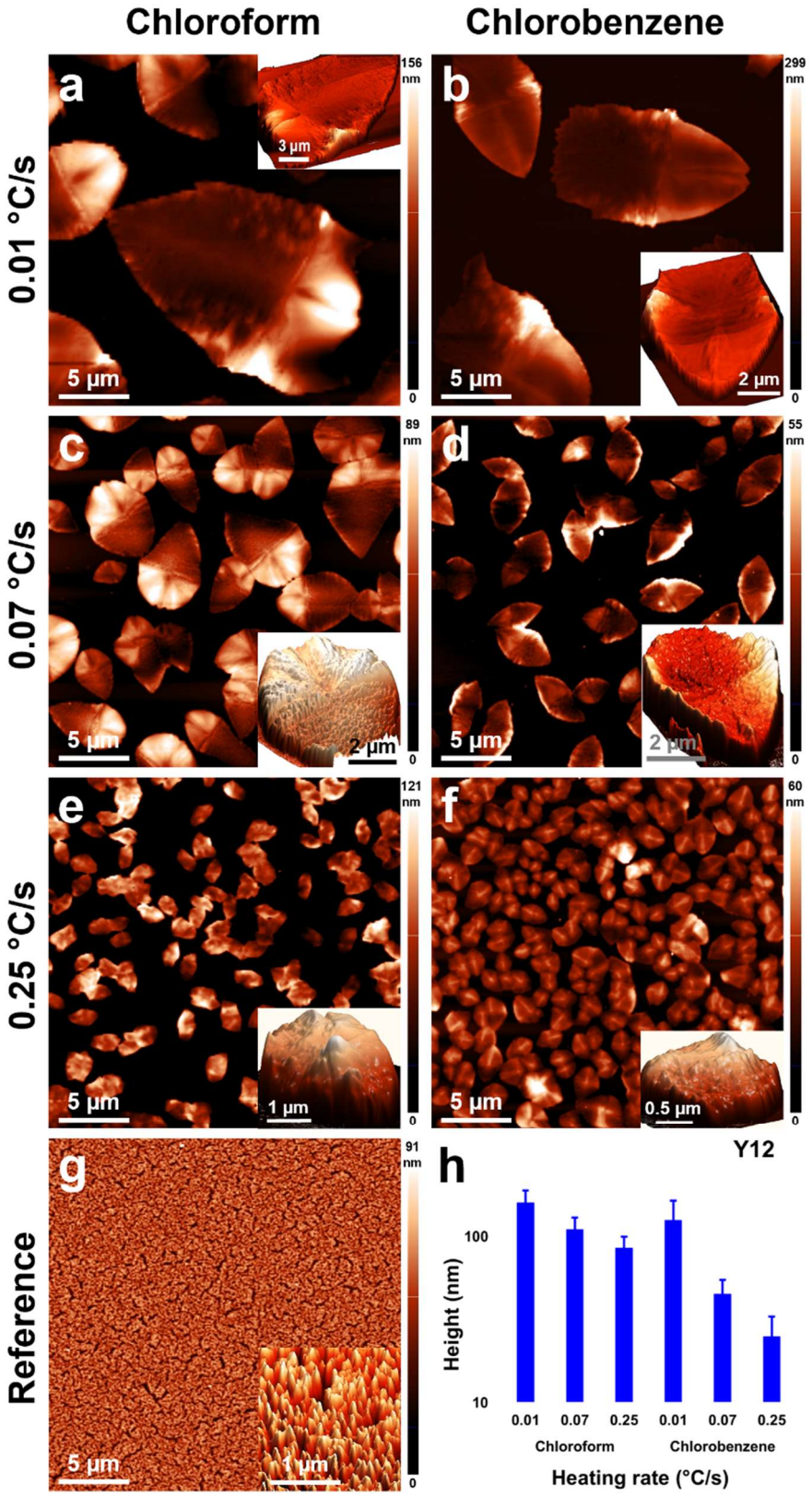

Figure 3.3 (a-g) AFM images of Y12 films exposed to chloroform (a, c, e) and chlorobenzene (b, d, f) vapors. Vapors were extracted at a film annealing rate of 0.01 °C/s (a-b), 0.07 °C/s (c-d) and 0.25 °C/s (e-f), respectively. (g) Surface of a reference Y12 film. Insets represent 3D views of the corresponding crystals. (h) Average height of crystals formed in chloroform and chlorobenzene, as a function of the film annealing rate. Image reproduced with permission from ref. [1].

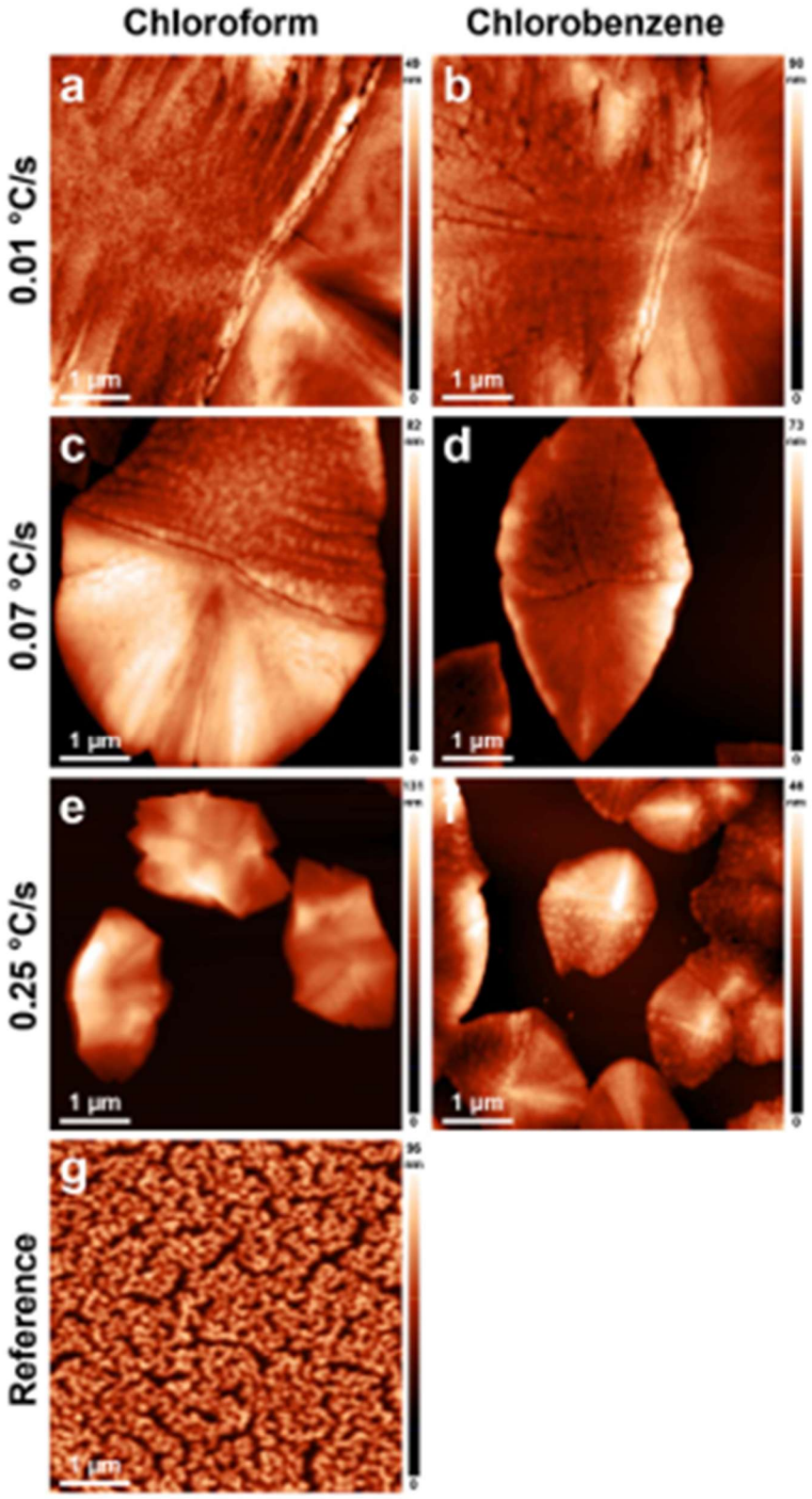

Figure 3.4 (a-g) AFM micrographs depicting the surface of thin films of Y12 processed via C SVA in chloroform (a, c, e) and chlorobenzene (b, d, f), while evaporating solvent vapors at a sample annealing rate of: 0.01 °C/s (a-b), 0.07 °C/s (c-d) and 0.25 °C/s (e-f), respectively. The surface of the corresponding as spin-cast (i.e., unexposed) Y12 film is shown in (g) for comparison. Image reproduced with permission from ref. [1].

3.1.2 Absorption spectra of films processed via C-SVA

To investigate whether the ordering process of Y12 molecules into acorn-shaped crystals induces any changes in their optoelectronic properties, we compared the absorbance characteristics of these crystals, seen in Figure 3.3a, the irregular microstructures of the Y12 reference film, presented in Figure 3.3g. The results of this comparison are presented in Figure 3.4, which displays the corresponding absorption spectra for the two samples.

The absorption spectrum of the Y12 reference film only reveals a main peak at a wavelength of 825 nm. In contrast, Y12 crystals display a significant red shift of 18 nm, moving the main peak to 843 nm. Additionally, in the spectrum for Y12 crystals a second peak, positioned at 734 nm, emerges. The increased strength of this second peak upon C-SVA processing is further clearly highlighted in Figure 3.5, where we have included partial peak fittings of the two groups of absorption peaks located at 734 nm and 825/843 nm. The observed intensity ratio between these two peaks is 1.12.

This notable change in the absorption spectrum points towards the high molecular ordering within the Y12 crystals. This effect is similar to a behavior previously observed in conjugated polymer single crystals [51]. There, a significant red shift of the main absorption peak, accompanied by a larger than 1 intensity ratio between peaks situated at longer and shorter wavelengths, indicates a high level of molecular ordering and full planarization of macromolecules.

Additionally, it is worth mentioning that the spectrum obtained for Y12 crystals exhibits a slight hollow shape on the descending edge at approximately 850 nm. This is an equipment generated artifact, rather than a property of the acorn-shaped crystals.

Overall, these results highlight the influence of the molecular structure’s organization on the optoelectronic properties of the Y12 films, indicating that by the formation of the ordered acorn-like crystals a comparison to an already known phenomenon seen in conjugated polymer single crystals can be drawn, resulting in a closer step in our understanding of the underlying physical mechanisms, which can hopefully lead to useful applications in electronic devices.

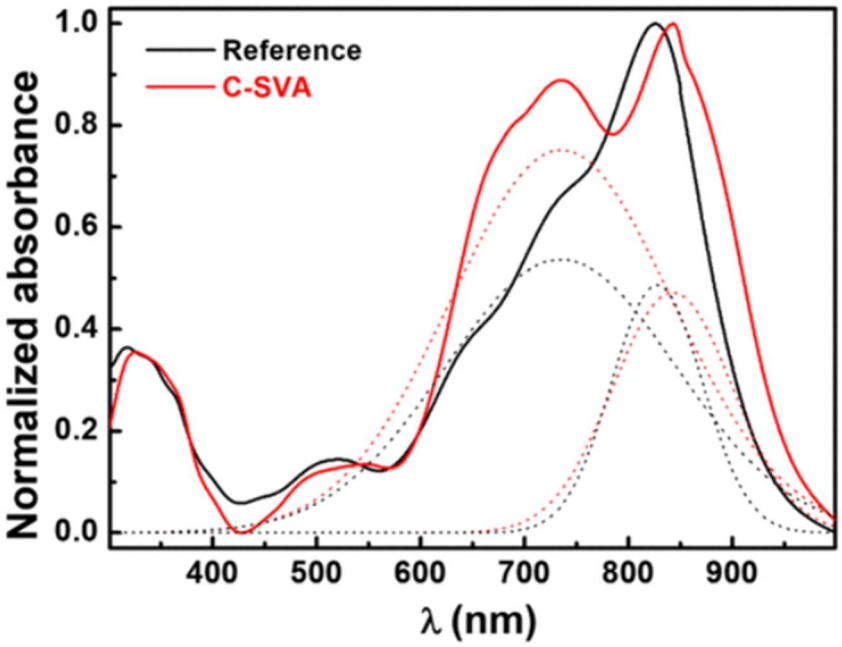

Figure 3.5 Normalized UV–vis absorption spectra of a Y12 film before (black) and after (red) its exposure to chloroform vapors (extracted at a film annealing rate of 0.01 °C/s). Dotted red lines correspond to the Gaussian fits of the 734 nm and 843 nm peaks, respectively, recorded for the Y12 film exposed to chloroform vapors via C-SVA. Dotted black lines represent the Gaussian fits of the weak shoulder at 734 nm and the 825 nm peak, respectively, recorded for the reference Y12 film. Image reproduced with permission from ref. [1].

3.1.3 Optical micrographs of films processed via thermal annealing

To gain an even deeper understanding of developing Y12 crystals with enhanced properties, we employed thermal annealing on the as spin-cast films by heating them to 260 ºC. As expected, this thermal treatment led to the melting of Y12, with the melting point being previously determined by differential scanning calorimetry measurements being approximately 273 ºC [52]. However, after reaching the melting point, the film dewetted and Y12 melt was pushed into irregularly shaped droplets, as illustrated in Figure 3.6. In such circumstances, crystallization could not even be induced at lower temperatures. The only visible formations are irregular structures within the dewetted droplets. This result highlights that while thermal annealing is known for organizing materials, it ultimately disrupted the film and failed to promote the growth of crystal structures.

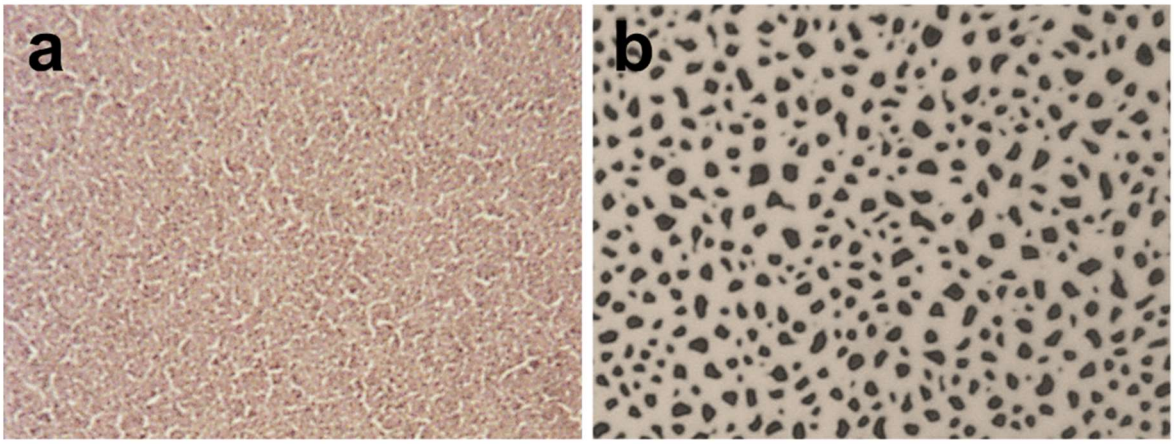

Figure 3.6 (a-b) Optical micrographs depicting the surface of a thin film of Y12 fabricated by spin-casting from a chloroform solution (a) that was thermally annealed at 260 °C for about 2 minutes (b). The size of both micrographs is 60×45 μm^2. Image reproduced with permission from ref. [1].

3.2 Y12 films fabricated by convective self-assembly

Lastly, we tried fabricating the films by employing the CSA method described above or in more detail in reference [47], because of its utilization for inducing ordering in polymer films. However, regardless of the film deposition speed or type of solvent used in the initial solution, the only results were either various densities of randomly distributed fibrillar structures of sizes ranging from just a few micrometers to several tens of micrometers (Figure 3.7), or agglomerations of Y12 aggregates/fibrils (Figure 3.8). As can be seen the formation of Y12 crystals did not appear.

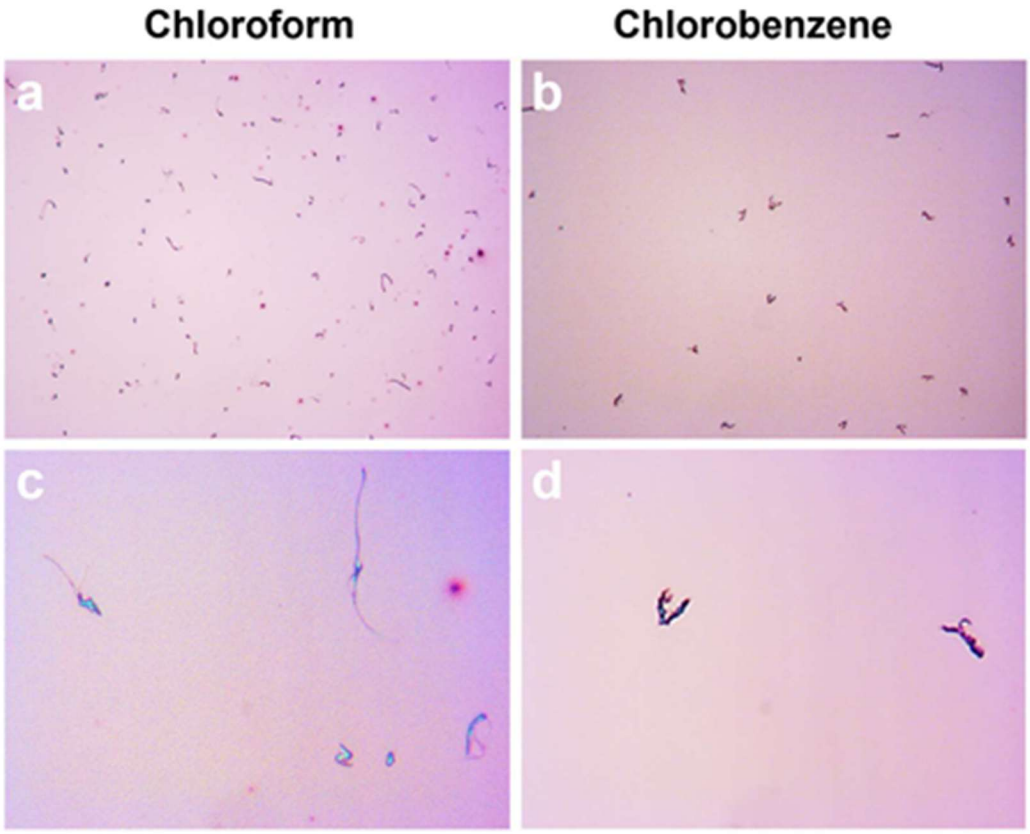

Figure 3.7 Optical micrographs depicting the surface of thin films of Y12 fabricated via convective self-assembly from chloroform (a, c) and chlorobenzene (b, d) solutions, while utilizing a deposition speed of 500 µm/s. The size of micrographs shown in (a-b) is 480×360 µm^2 that of micrographs depicted in (c-d) is 120×90 µm^2. Image reproduced with permission from ref. [1].

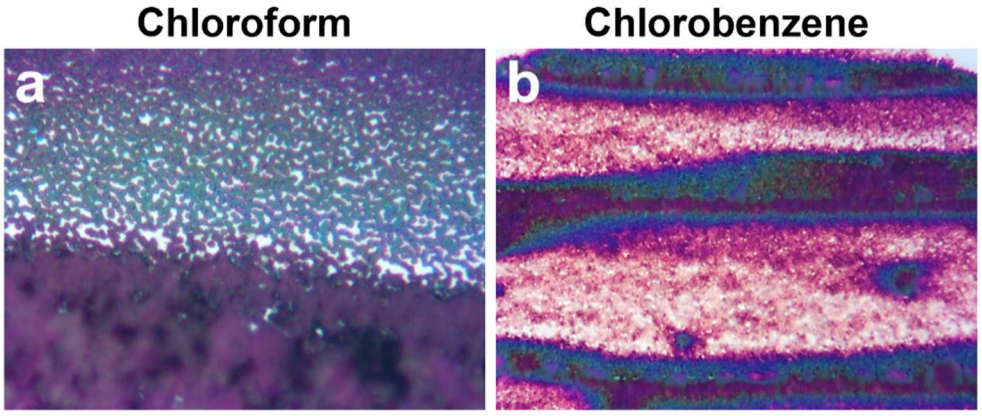

Figure 3.8 (a-b) Optical micrographs depicting the surface of thin films of Y12 fabricated via convective self-assembly from chloroform (a) and chlorobenzene (b) solutions, while utilizing a deposition speed of only 10 µm/s. The size of both micrographs is 120×90 µm^2. Image reproduced with permission from ref. [1].

3.3 Conclusions

In this chapter, Y12 spin-cast thin films were exposed to chloroform or chlorobenzene solvent vapors, followed by their swelling and deswelling process at controlled evaporation rates. Less and bigger crystals formed at low evaporation rates, whereas more crystals formed at high evaporation rates, but these were smaller. These were the only circumstances which induced crystallization, as could be seen in the failed attempts with convective self-assembly and thermal annealing. This ultimately demonstrates that generating Y12 crystals is possible only under very certain conditions and it explains why they have not been obtained until now.

NOTE: Parts of this chapter were either utilized or adapted from the article that was previously published by us: [1]

Chapter 4

Processing and analysis of Y6 films

To have an even more complete overview of the formation of crystals, we replaced Y12 with its Y6 counterpart. The main quest was checking whether it was possible to obtain crystals of higher quality, such as single crystals, from this family of NFAs via the C-SVA processing method. Intermolecular interactions are promoted by both systems, but the difference between them is that Y12 has two butyloctyl side chains, whereas Y6 has two ethylhexyl chains connected to its core structure. In the case of Y6 this means a decrease in solubility which implies the range of processing methods for obtaining crystals is even more narrow compared to Y12. Nonetheless this study might prove relevant in terms of crystals density and quality.

4.1 Y6 films fabricated by spin-casting

4.1.1 Optical micrographs and AFM images of films processed via C-SVA

As illustrated in Figure 4.1, the best Y6 crystals were obtained when chloroform and chlorobenzene vapors were gradually extracted at a very slow rate, to be more exact, at 0.01 ºC/s. We were surprised to find crystals exhibiting not only elongated hexagonal shapes but also a consistent molecular arrangement. This high order of Y6 molecules strongly suggests the presence of single crystals.

Our hypothesis is that the relatively lower solubility and processability of Y6 molecules allowed an efficient nucleation and development into large single crystals. This process seems to be facilitated only when the time period was extended enough under highly diluted conditions of the swollen rich “film-solutions”. Specifically, this seems to exclusively occur at film annealing rates of 0.01 ºC/s as depicted in Figure 4.1a,b, as well as in Figure 4.2.

A closer analysis showed that the corresponding densities of single crystals in chloroform and chlorobenzene were $4.86 \times 10^{-4}/\mu m^2$ and $1.16 \times 10^{-4}/\mu m^2$, respectively. It is to be noted that these densities are almost an order of magnitude lower than those found for Y12 corresponding crystals, reflecting that the crystallization process of the two materials differs significantly. Moving on to matters related to the dimensions of the crystals, the length to width ratio has been found to be approximately 14 µm to 5.7 µm for chloroform and 31 µm to 10.4 µm for chlorobenzene, as can be seen in Figure 4.1h.

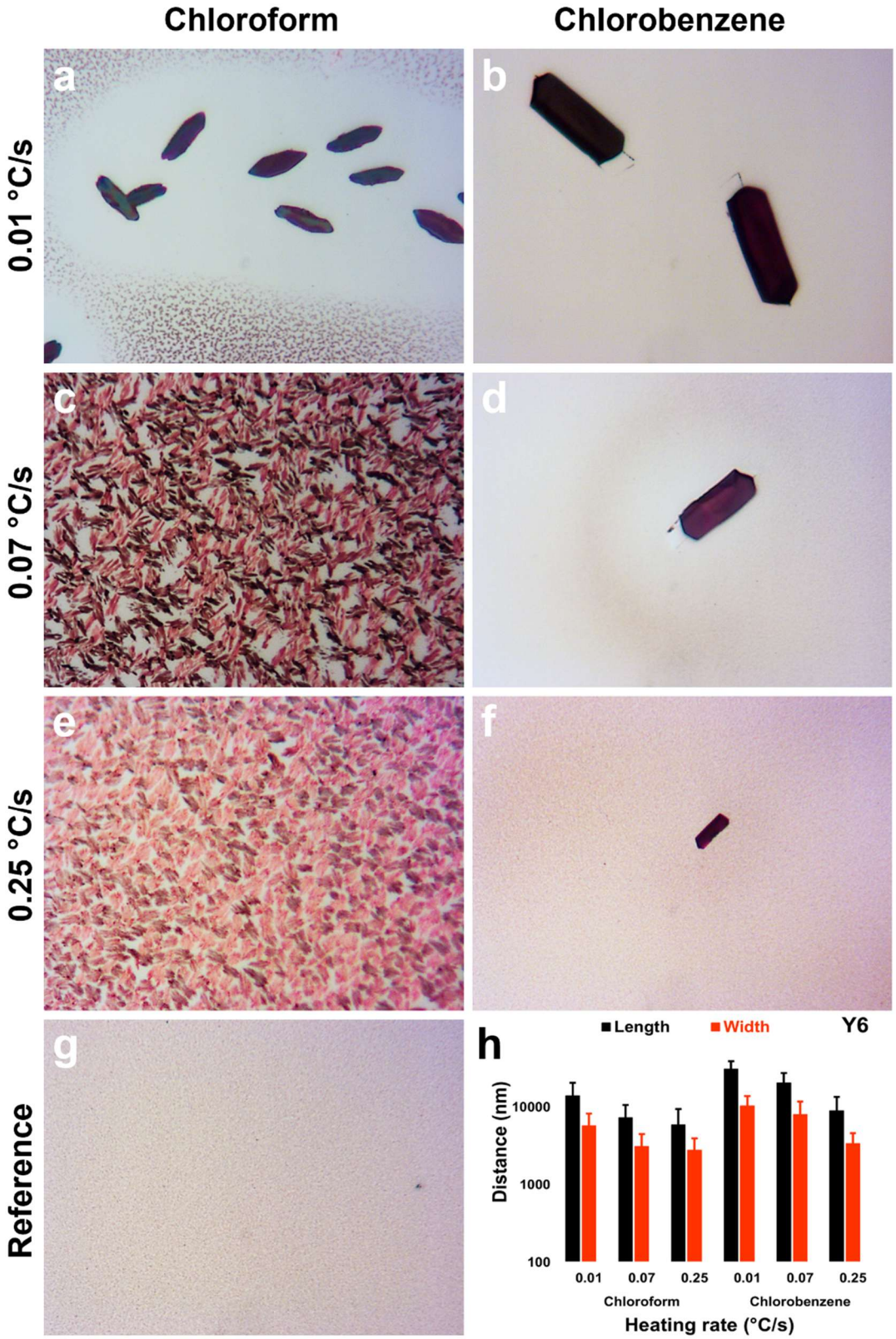

Figure 4.1 (a-f) Optical micrographs of Y6 films exposed to chloroform (a, c, e) and chlorobenzene (b, d, f) vapors. Vapors were extracted at a film annealing rate of 0.01 °C/s (a-b), 0.07 °C/s (c-d) and 0.25 °C/s (e-f), respectively. (g) Surface of a reference Y6 film. Size of all images is 120×90 μm^2. (h) Average length and width of Y6 crystals formed in chloroform and chlorobenzene as a function of film heating rate. Image reproduced with permission from ref. [1].

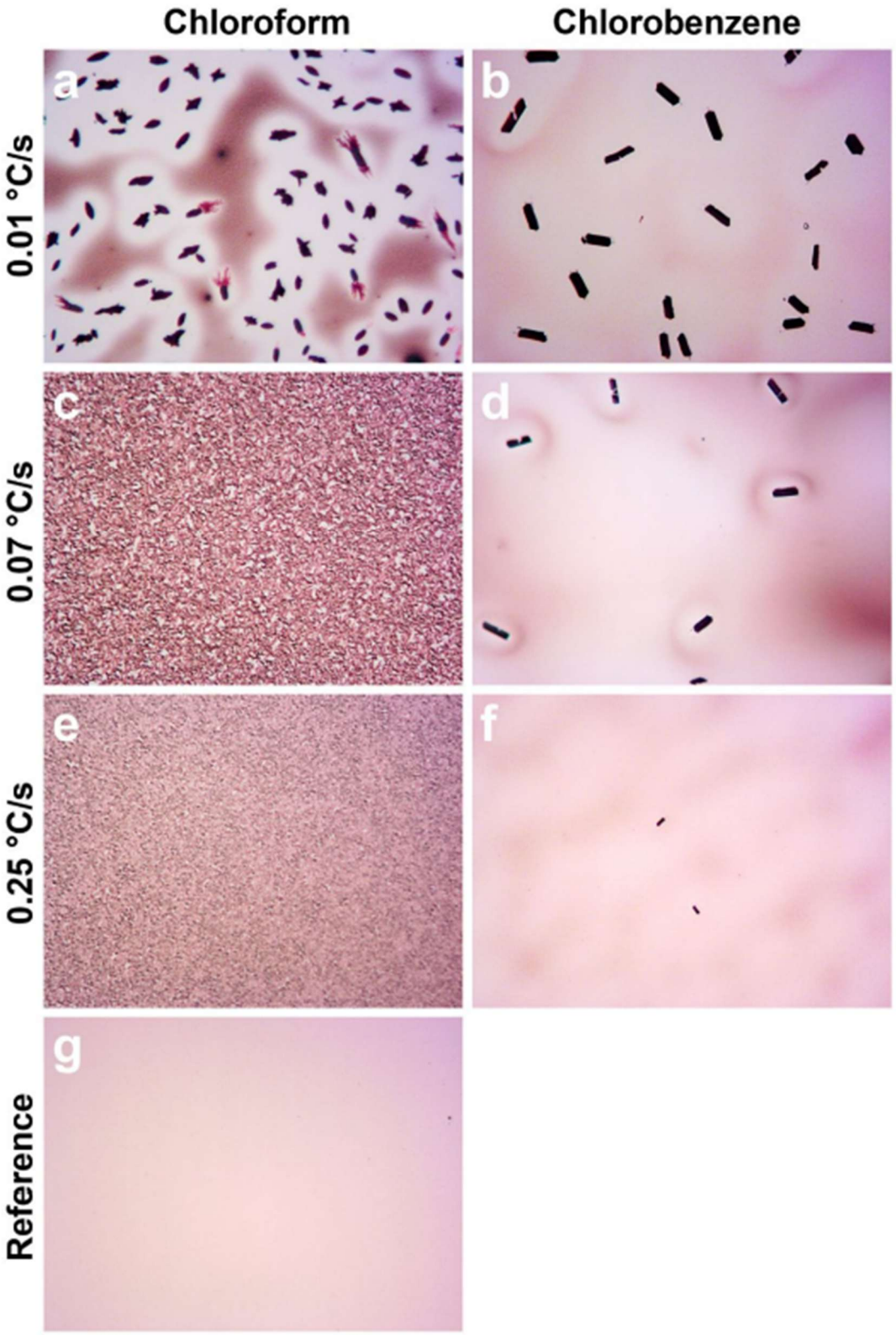

Figure 4.2 Optical micrographs depicting the surface of thin films of Y6 processed via C-SVA in chloroform (a, c, e) and chlorobenzene (b, d, f), while evaporating solvent vapors at a sample annealing rate of: 0.01 °C/s (a-b), 0.07 °C/s (c-d) and 0.25 °C/s (e-f), respectively. The surface of the corresponding as spin-cast Y6 film is shown in (g) for comparison. The size of all micrographs is 480×360 μm^2. Image reproduced with permission from ref. [1].

The hypothesis mentioned above was further supported by the observation of fewer and smaller crystal formation at higher chlorobenzene evaporation rates. To be more specific, our measurements revealed crystal densities for Y6 films exposed to annealing rates of 0.07 ºC/s and 0.25 ºC/s to be 2.43 × 10^{-4}/μm^2 and 1.16 × 10^{-5}/μm^2, respectively. Furthermore, the average length/width dimensions of the single crystals suffered a decrease from 20.5/8 μm to 9/3.4 μm, accentuating the different stages that appear in the development of crystals. Another striking detail can be visualized in Figure 4.1c,e, namely when chloroform vapors were used in the annealing process, no single crystals formed. Instead, the employment of these more volatile vapors resulted in a plethora of less ordered structures spread on the entire surface. This highlights a new dependence that might be important for future applications: the relation between volatility and crystal nucleation. As expected, no crystalline structures were detected in the reference Y6 film, only small irregular aggregates, as depicted in Figure 4.1g.

Lastly, when employing the more volatile chloroform vapors – even at the lowest film annealing rate of 0.01 ºC/s – deviations from the hexagonal morphology were observed, as shown in Figure 4.2a. The reason behind this could be the incorporation of Y6 molecules with different molecular conformations, thus, losing the privilege of being single crystals. Additionally, in contrast to Y12 crystals, Y6 crystals were consistently surrounded by regions consisting of submicrometric irregular structures, developed under higher concentration conditions of Y6 (Figure 4.1a,b,d,f). This seems to be a direct consequence of the lower crystal density, which leaves various Y6 molecules in the surrounding "film-solution" free and available for potential further structural formation during subsequent deswelling stages.

Hand in hand with the obtained results for Y12 crystals, the AFM technique further confirmed that Y6 single crystals were three-dimensional objects displaying an elongated hexagonal morphology, as illustrated in Figure 4.3 and Figure 4.4. As in the case of Y12, these pronounced crystal shapes cannot be compared to the reference film, which is covered by the hundred nanometers sized structures, as depicted in Figure 4.3g and Figure 4.4g. A clear trend can be seen regarding the average height to single crystals in relation to the rate of film annealing, namely an increase in the chlorobenzene evaporation rate causes a decrease in the height of Y6 single crystals from 1100 nm to 605 nm, and then to just 290 nm (Figure 3.3h). A similar behavior can be observed when using chloroform vapors, with the average height declining from 395 nm to 108 nm, and further down to 55 nm. Single crystals were only detected for the lowest chloroform evaporation rate, also in this case.

When evaporating the solvent more quickly, the film surfaces were no longer covered in single crystals; rather, they were filled with several/few micrometers long/wide bundles. These

bundles as shown in Figure 4.3c,e have a few micrometer-sized substructures in their composition and most exhibit an elongated hexagonal morphology (Figure 4.4c,e).

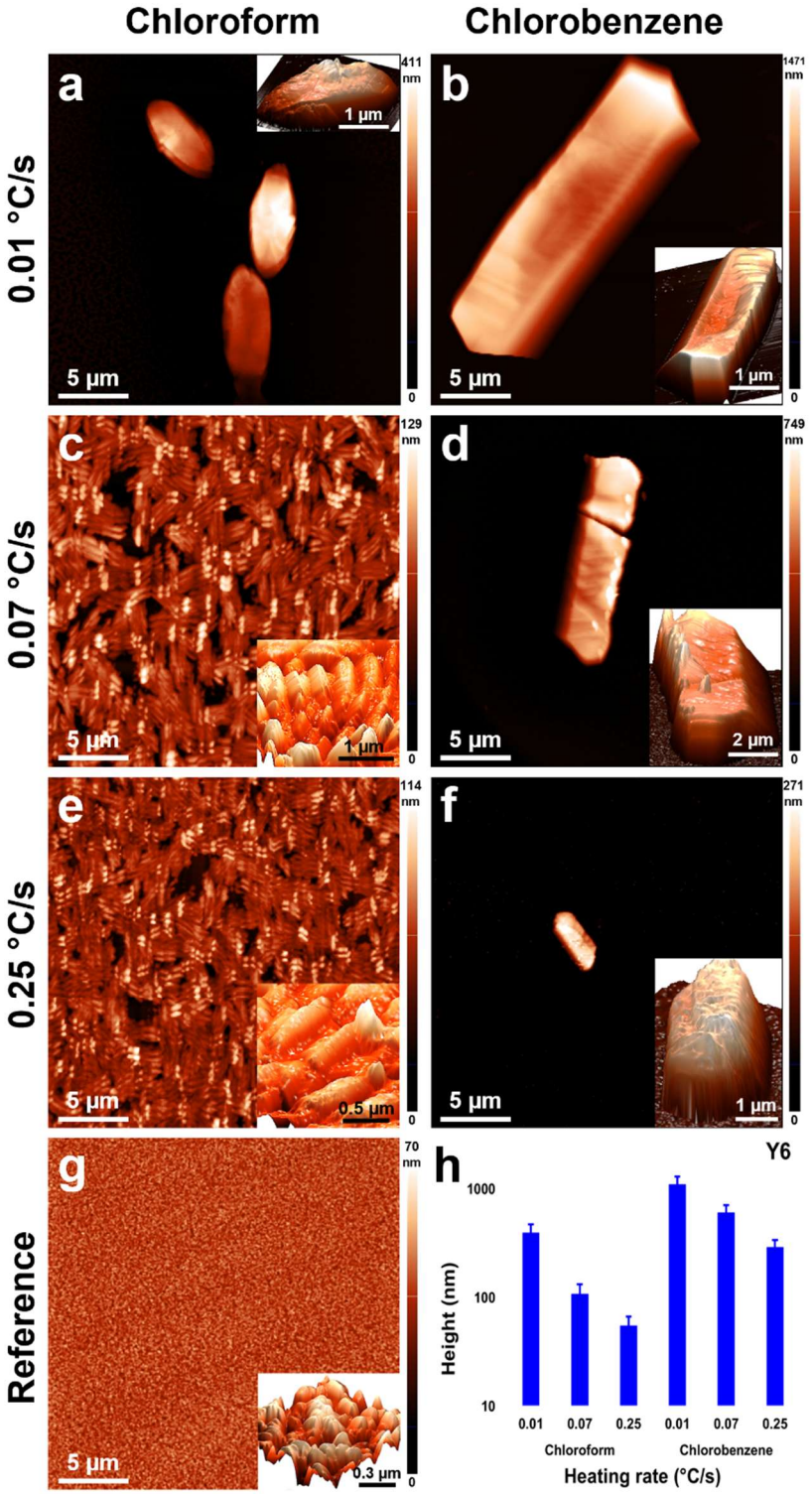

Figure 4.3 (a-g) AFM images of Y6 films exposed to chloroform (a, c, e) and chlorobenzene (b, d, f) vapors. The latter were evaporated at a film annealing rate of 0.01 °C/s (a-b), 0.07 °C/s (c-d) and 0.25 °C/s (e-f), respectively. (g) Surface of a reference Y6 film. Each inset represents a 3D view of the corresponding structures. (h) Average height of crystals formed in chloroform and chlorobenzene, as a function of the heating rate. Image reproduced with permission from ref. [1].

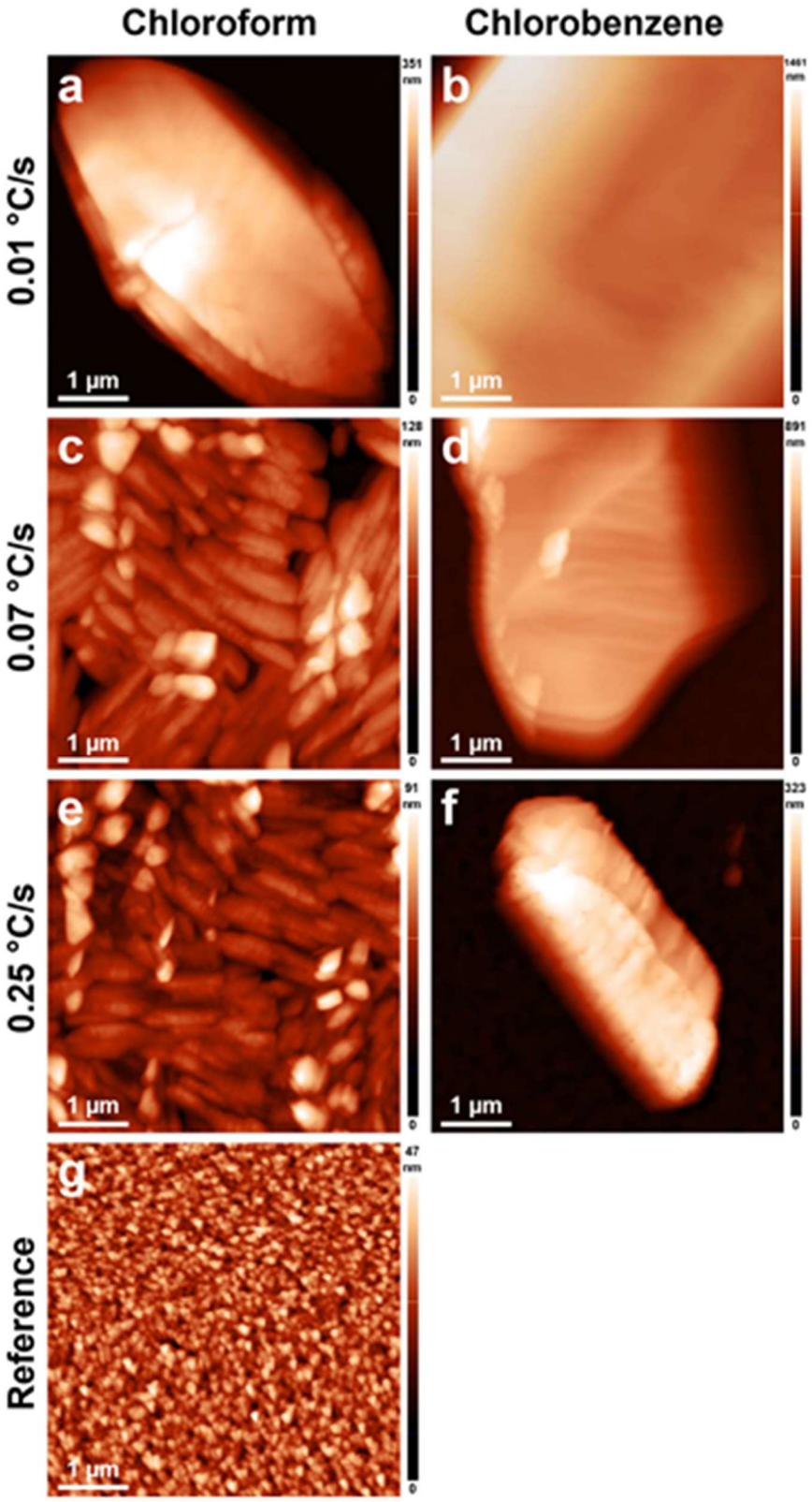

Figure 4.4 (a-g) AFM micrographs depicting the surface of thin films of Y6 processed via C-SVA in chloroform (a, c, e) and chlorobenzene (b, d, f), while evaporating solvent vapors at a sample annealing rate of: 0.01 °C/s (a-b), 0.07 °C/s (c-d) and 0.25 °C/s (e-f), respectively. The surface of the corresponding as spin-cast reference Y6 film is shown in (g) for comparison. Image reproduced with permission from ref. [1].

4.1.2 Absorption spectra of films processed via C-SVA

The next aspect that was analyzed was the change in absorbance resulting from the orderly arrangement of the Y6 molecules into elongated hexagonal shaped crystals after undergoing C-SVA post-treatment. The exact procedure consisted of comparing the absorbance spectra of the reference film shown in Figure 4.1g with the processed films containing single crystals, depicted in Figure 4.1a., as can be seen in Figure 4.5.

The measurements revealed that the Y6 reference film exhibited only one single prominent absorption peak at 840 nm, whereas the Y6 single crystals resulted in a more complex absorption spectra, containing two absorption peaks at 840 nm and 738 nm. In contrast to the Y12 crystals, when working with Y6 no clear spectral shift of the main peak was visible, whereas the intensity ratio between the two located peaks is slightly higher for the latter, with a value reaching 1.33, which indicates a high degree of molecular ordering [51]. Although we anticipated observing the spectral red shift of the main absorbance peak, a plausible reason for its absence may be attributed to the small and limited number of crystals existent on the surface, with their surroundings consisting of the majority of less ordered Y6 crystalline structures.

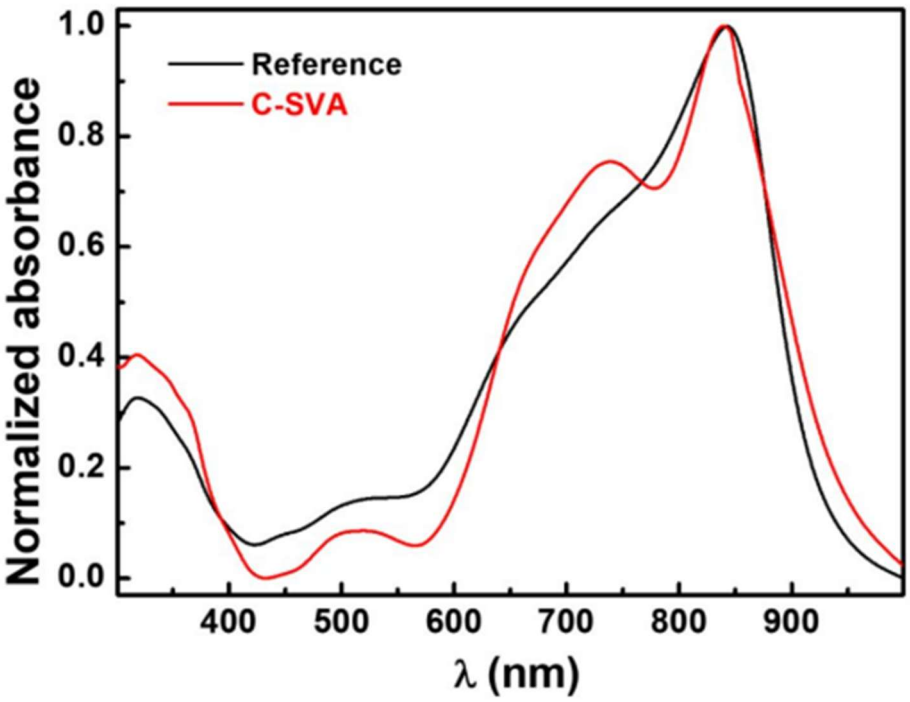

Figure 4.5 Normalized UV-vis absorption spectra recorded for a Y6 thin film before (black) and after (red) its exposure via C-SVA to chloroform vapors. Note that the evaporation of chloroform vapors was conducted at a sample annealing rate of 0.01 °C/s. Image reproduced with permission from ref. [1].

4.1.3 Optical micrographs of films processed via thermal annealing

The next attempt of achieving crystals was by applying the thermal annealing processing method on Y6 films and heating them to 260 ºC. As expected, this thermal treatment led to the melting of Y6, with the melting point being previously determined by differential scanning calorimetry measurements and ranging between slightly less than 290 ºC and 298 ºC [52], [53]. The melting resulted in a series of events that included film dewetting and formation of irregular droplets, depicted in Figure 4.6. Similar to Y12, no Y6 crystals were produced in the thermal annealing process.

These results reinforce the statement that fabricating Y6 is extremely challenging. The nucleation and growth are induced only in very specific conditions, namely when extracting the solvent vapors at a very slow pace.

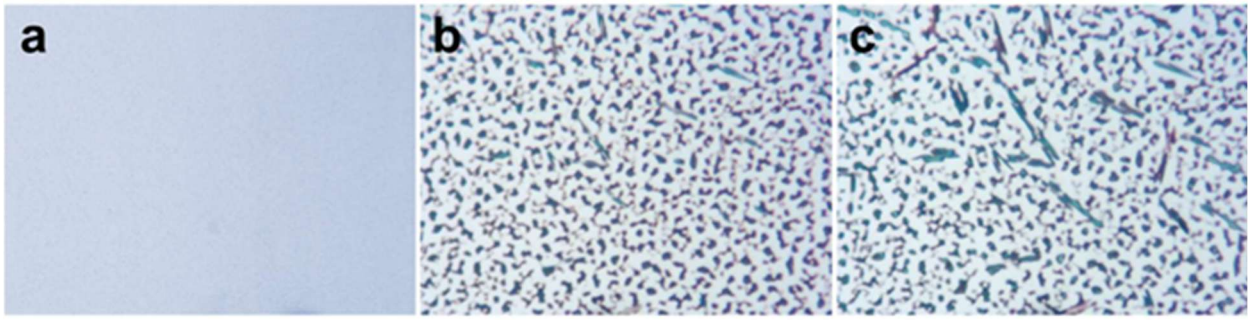

Figure 4.6 (a-c) Optical micrographs depicting the surface of a thin film of Y6 fabricated by spin-casting from a chloroform solution (a) that was thermally annealed at 260 °C for about 2 minutes (b) and kept at 180 °C for another 15 minutes. The size of all micrographs is 120×90 μm^2. Image reproduced with permission from ref. [1].

4.2 Y6 films fabricated by convective self-assembly

Lastly, similar to the case of the Y12 system, convective self-assembly of Y6 led to two results depending on the deposition speed employed. Using higher deposition speeds led to fibrillar micrometer-sized structures, the density of which exhibited significant variability, which can be clearly seen in Figure 4.7. On the other hand, when using low deposition speeds, agglomerations of Y6 aggregates were either randomly distributed or arranged in parallel stripes, as illustrated in Figure 4.8.

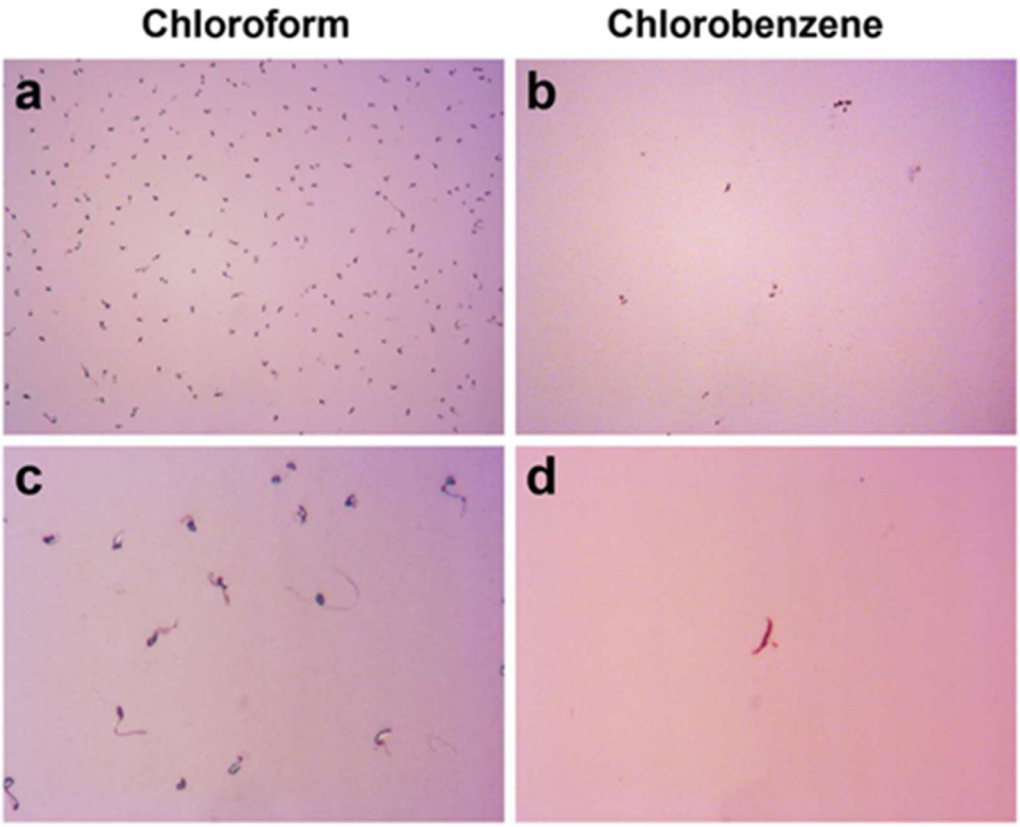

Figure 4.7 Optical micrographs depicting the surface of thin films of Y6 fabricated via convective self-assembly from chloroform (a, c) and chlorobenzene (b, d) solutions, while utilizing a deposition speed of 500 µm/s. The size of micrographs shown in (a-b) is 480×360 µm^2, while that of micrographs depicted in (c-d) is 120×90 µm^2. Image reproduced with permission from ref. [1].

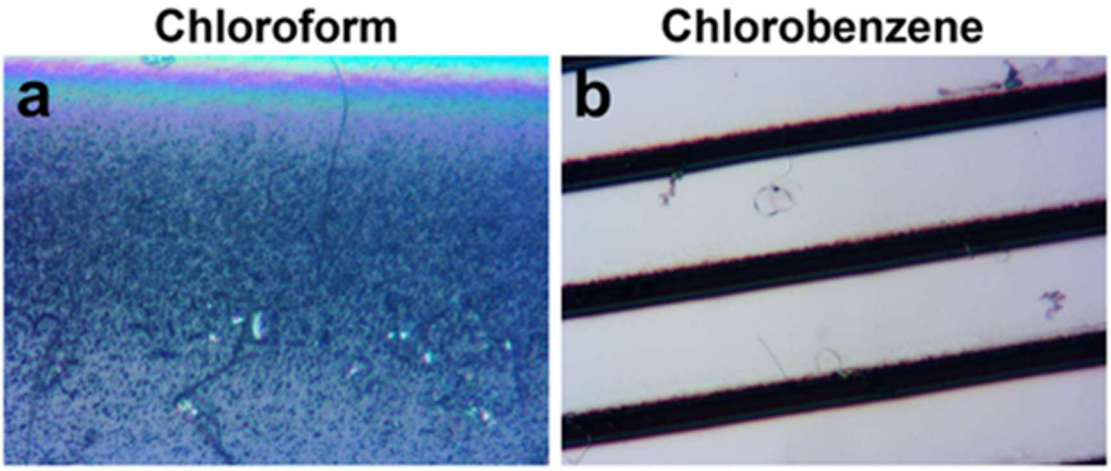

Figure 4.8 (a-b) Optical micrographs depicting the surface of thin films of Y6 fabricated via convective self-assembly from chloroform (a) and chlorobenzene (b) solutions, while utilizing a deposition speed of only 10 µm/s. The size of both micrographs is 120×90 µm^2. Image reproduced with permission from ref. [1].

4.3 Conclusions

In this chapter, Y6 spin-cast thin films were subjected to either chloroform or chlorobenzene solvent vapors. This procedure was accompanied by the swelling and deswelling of the films at precisely controlled evaporation rates. At lower evaporation rates, single crystals were produced, whereas higher evaporation rates resulted in a plethora of less ordered structures spread on the entire surface. These specific conditions were the only ones which favored crystallization, as could be seen in the unsuccessful attempts involving convective self-assembly or thermal annealing. This strengthens our premise, namely that the formation of Y6 and Y12 crystals is achievable only under very particular conditions, which clarifies why such crystals have not been generated previously.

NOTE: Parts of this chapter were either utilized or adapted from the article that was previously published by us: [1]

General conclusions

In this study, we fabricated novel crystals, including single crystals, of Y6 and Y12 NFAs for the first time. This was accomplished by exposing both materials to generous amounts of solvent vapors by employing the C-SVA processing technique, which was used in other studies to self-assemble [38] and crystallize [39] various copolymers [40] and biopolymers [41].

The main procedure involves exposing the thin films, fabricated by spin-casting Y6 and Y12 solutions onto ozone treated clean silicon wafers, to solvent vapors. The chosen solvents were chloroform and chlorobenzene, and the effect of the vapor treatment led to the phenomenon known as film swelling, in which the solid films were transformed into quasi two dimensional "film-solutions". In this stage a change in the interference colors was visible with the naked eye and was followed by a morphological alteration into a more orderly structure through crystallization. The final step consisted of gradually increasing the temperature until the films were completely dry.

As revealed by optical microscopy, convective self-assembly for both materials resulted either in various densities of randomly distributed fibrillar structure with varying sizes, or agglomerations of Y6 or Y12 aggregates/fibrils, respectively. In this case no Y6 and Y12 crystals formed. Moreover, thermal annealing on the as spin-cast Y6 and Y12 films by heating them to 260 ^{o}C let to the melting of both Y6 and Y12. While this was expected because of their previously determined melting points by differential scanning calorimetry in the literature ranging between 290-298 ^{o}C and being at 273 ^{o}C for the latter, no Y6 and Y12 crystals were obtained through thermal annealing. To be noted, is the fact that after reaching the melting point, the films dewetted and the melt was pushed into irregularly shaped droplets and crystallization was not induced even at lower temperatures. However, within the dewetted droplets some irregular structures could be seen forming. These results highlighted the difficulty of obtaining Y6 and Y12 crystals and the importance of the peculiar C-SVA circumstances necessary to generate Y6 and Y12 crystals.

Returning to the discussion about the C-SVA processed films, optical and atomic force microscopy uncovered that the more soluble Y12 system produced a great variation of dense, acorn-shaped crystals that were visible on the surfaces of the films. Both crystal densities and sizes were found to be highly dependent on the specific type of solvents used during the process, as well as the solvent evaporation rate which was influenced by the film annealing rates. Y6, on the other hand, is less soluble and processing resulted in less dense elongated hexagonal single crystals. It is to be noted that crystals were obtained only for the slowest solvent evaporation rate in chloroform, as opposed to chlorobenzene which also induced crystallization at higher evaporation

rates, although the density and size were significantly smaller. Importantly, the crystallization did not take place in the reference films for both systems.

Although the physical process in the C-SVA method is mainly the same for all its applications, it has one particularly challenging aspect, namely finding the right temperature to force a condensation onto the film samples. This implies gradually lowering the temperature and the volatility of the used solvents also plays a crucial role, as could be seen in this work by using chloroform which is more volatile than chlorobenzene. The surprisingly low temperature found for the systems studied in this work was between 15 ºC and 20 ºC.

Furthermore, UV-vis spectroscopy gave us an even better insight into the Y6 and Y12 crystals. The solvent treated films exhibited an additional absorption peak and in the case of Y12 this was accompanied by a red shift of the main peak. In other words, compared to reference films, due to the increase in molecular ordering, these systems exhibit puzzling absorption properties.

Future studies are needed to precisely determine the crystal packing of these structures, for us to determine whether these crystals are model systems for evaluating and optimizing optoelectronic properties of Y6 and Y12 NFAs. Before their integration into devices like OFETs, conducting electrical performance testing such as charge mobility measurements or incorporating the crystals into OFET configurations, would be helpful for precisely establishing a relationship between crystal formation and optoelectronic performance. Moreover, by taking advantage of the well-known relationship between microstructure, processing and resulting properties, these highly ordered crystals could be integrated into OSCs. Their ordered morphological arrangement could promote a more uniform donor-acceptor phase within the active layer, potentially leading to a higher phase purity and reduced recombination losses, ultimately enhancing overall device efficiency.

References

[1] Y. Cotoarbă, O. Todor-Boer, and I. Botiz, "Crystals of Nonfullerene Acceptors Generated by Rich Exposure to Solvent Vapors," *Cryst. Growth Des.*, vol. 25, no. 8, pp. 2337–2346, Apr. 2025, doi: 10.1021/acs.cgd.5c00192.

[2] G. Li, R. Zhu, and Y. Yang, "Polymer solar cells," *Nat. Photonics*, vol. 6, no. 3, pp. 153–161, Mar. 2012, doi: 10.1038/nphoton.2012.11.

[3] M. Graetzel, R. A. J. Janssen, D. B. Mitzi, and E. H. Sargent, "Materials interface engineering for solution-processed photovoltaics," *Nature*, vol. 488, no. 7411, pp. 304–312, Aug. 2012, doi: 10.1038/nature11476.

[4] C. J. Brabec, M. Heeney, I. McCulloch, and J. Nelson, "Influence of blend microstructure on bulk heterojunction organic photovoltaic performance," *Chem. Soc. Rev.*, vol. 40, no. 3, pp. 1185–1199, 2011, doi: 10.1039/C0CS00045K.

[5] T. Kumari *et al.*, "Bilayer layer-by-layer structures for enhanced efficiency and stability of organic photovoltaics beyond bulk heterojunctions," *Cell Rep. Phys. Sci.*, vol. 5, no. 6, p. 102027, Jun. 2024, doi: 10.1016/j.xcrp.2024.102027.

[6] T. Benanti and D. Venkataraman, "Organic Solar Cells: An Overview Focusing on Active Layer Morphology," *Photosynth. Res.*, vol. 87, pp. 73–81, Feb. 2006, doi: 10.1007/s11120-005-6397-9.

[7] T. Kumari, M. Moon, S.-H. Kang, and C. Yang, "Improved efficiency of DTGe(FBTTh2)2-based solar cells by using macromolecular additives: How macromolecular additives versus small additives influence nanoscale morphology and photovoltaic performance," *Nano Energy*, vol. 24, pp. 56–62, Jun. 2016, doi: 10.1016/j.nanoen.2016.03.026.

[8] "Pseudo-bilayer architecture enables high-performance organic solar cells with enhanced exciton diffusion length | Nature Communications." Accessed: Mar. 20, 2025. [Online]. Available: https://www.nature.com/articles/s41467-020-20791-z

[9] L. Tian, C. Liu, and F. Huang, "Recent progress in side chain engineering of Y-series non-fullerene molecule and polymer acceptors," *Sci. China Chem.*, vol. 67, no. 3, pp. 788–805, Mar. 2024, doi: 10.1007/s11426-023-1774-6.

[10] Y. He and Y. Li, "Fullerene derivative acceptors for high performance polymer solar cells," *Phys. Chem. Chem. Phys.*, vol. 13, no. 6, pp. 1970–1983, 2011, doi: 10.1039/C0CP01178A.

[11] W. Li *et al.*, "Mobility-Controlled Performance of Thick Solar Cells Based on Fluorinated Copolymers," *J. Am. Chem. Soc.*, vol. 136, no. 44, pp. 15566–15576, Nov. 2014, doi: 10.1021/ja5067724.

[12] X. Liu, W. Shen, R. He, Y. Luo, and M. Li, "Strategy to Modulate the Electron-Rich Units in Donor–Acceptor Copolymers for Improvements of Organic Photovoltaics," *J. Phys. Chem. C*, vol. 118, no. 31, pp. 17266–17278, Aug. 2014, doi: 10.1021/jp503248a.

[13] P. Cheng and X. Zhan, "Stability of organic solar cells: challenges and strategies," *Chem. Soc. Rev.*, vol. 45, no. 9, pp. 2544–2582, 2016, doi: 10.1039/C5CS00593K.

[14] Y. He, H.-Y. Chen, J. Hou, and Y. Li, "Indene−C60 Bisadduct: A New Acceptor for High-Performance Polymer Solar Cells," *J. Am. Chem. Soc.*, vol. 132, no. 4, pp. 1377–1382, Feb. 2010, doi: 10.1021/ja908602j.

[15] C. B. Nielsen, S. Holliday, H.-Y. Chen, S. J. Cryer, and I. McCulloch, "Non-Fullerene Electron Acceptors for Use in Organic Solar Cells," *Acc. Chem. Res.*, vol. 48, no. 11, pp. 2803–2812, Nov. 2015, doi: 10.1021/acs.accounts.5b00199.

[16] P. Cheng, G. Li, X. Zhan, and Y. Yang, "Next-generation organic photovoltaics based on non-fullerene acceptors," *Nat. Photonics*, vol. 12, no. 3, pp. 131–142, Mar. 2018, doi: 10.1038/s41566-018-0104-9.

[17] H. Zubair *et al.*, "A computational insight into enhancement of photovoltaic properties of non-fullerene acceptors by end-group modulations in the structural framework of INPIC molecule," *J. Mol. Graph. Model.*, vol. 126, p. 108664, Jan. 2024, doi: 10.1016/j.jmgm.2023.108664.

[18] J. Wang, Y. Xie, K. Chen, H. Wu, J. M. Hodgkiss, and X. Zhan, "Physical insights into non-fullerene organic photovoltaics," *Nat. Rev. Phys.*, pp. 1–17, Apr. 2024, doi: 10.1038/s42254-024-00719-y.

[19] Y. Cai *et al.*, "Vertically optimized phase separation with improved exciton diffusion enables efficient organic solar cells with thick active layers," *Nat. Commun.*, vol. 13, no. 1, p. 2369, May 2022, doi: 10.1038/s41467-022-29803-6.

[20] S. Holliday, "Synthesis and Characterisation of Non Fullerene Electron Acceptors for Organic Photovoltaics."

[21] E. Gutierrez-Fernandez, A. D. Scaccabarozzi, A. Basu, E. Solano, T. D. Anthopoulos, and J. Martín, "Y6 Organic Thin-Film Transistors with Electron Mobilities of 2.4 cm2 V−1 s−1 via Microstructural Tuning," *Adv. Sci.*, vol. 9, no. 1, p. 2104977, 2022, doi: 10.1002/advs.202104977.

[22] Y. Lin *et al.*, "An Electron Acceptor Challenging Fullerenes for Efficient Polymer Solar Cells," *Adv. Mater.*, vol. 27, no. 7, pp. 1170–1174, Feb. 2015, doi: 10.1002/adma.201404317.

[23] Y. Lin *et al.*, "A Facile Planar Fused-Ring Electron Acceptor for As-Cast Polymer Solar Cells with 8.71% Efficiency," *J. Am. Chem. Soc.*, vol. 138, no. 9, pp. 2973–2976, Mar. 2016, doi: 10.1021/jacs.6b00853.

[24] J. Sun *et al.*, "Dithieno[3,2- *b* :2′,3′- *d*]pyrrol Fused Nonfullerene Acceptors Enabling Over 13% Efficiency for Organic Solar Cells," *Adv. Mater.*, vol. 30, no. 16, p. 1707150, Apr. 2018, doi: 10.1002/adma.201707150.

[25] W. Li *et al.*, "Retarding the Crystallization of a Nonfullerene Electron Acceptor for High-Performance Polymer Solar Cells," *Adv. Funct. Mater.*, vol. 29, no. 5, p. 1807662, Feb. 2019, doi: 10.1002/adfm.201807662.

[26] G. Forti, A. Nitti, P. Osw, G. Bianchi, R. Po, and D. Pasini, "Recent Advances in Non-Fullerene Acceptors of the IDIC/ITIC Families for Bulk-Heterojunction Organic Solar Cells," *Int. J. Mol. Sci.*, vol. 21, no. 21, Art. no. 21, Jan. 2020, doi: 10.3390/ijms21218085.

[27] L. Nian *et al.*, "Ternary non-fullerene polymer solar cells with 13.51% efficiency and a record-high fill factor of 78.13%," *Energy Environ. Sci.*, vol. 11, no. 12, pp. 3392–3399, 2018, doi: 10.1039/C8EE01564C.

[28] J. Yuan *et al.*, "Single-Junction Organic Solar Cell with over 15% Efficiency Using Fused-Ring Acceptor with Electron-Deficient Core," *Joule*, vol. 3, no. 4, pp. 1140–1151, Apr. 2019, doi: 10.1016/j.joule.2019.01.004.

[29] B. Fan *et al.*, "Achieving over 16% efficiency for single-junction organic solar cells," *Sci. China Chem.*, vol. 62, no. 6, pp. 746–752, Jun. 2019, doi: 10.1007/s11426-019-9457-5.

[30] T. Yan, W. Song, J. Huang, R. Peng, L. Huang, and Z. Ge, "16.67% Rigid and 14.06% Flexible Organic Solar Cells Enabled by Ternary Heterojunction Strategy," *Adv. Mater.*, vol. 31, no. 39, p. 1902210, 2019, doi: 10.1002/adma.201902210.

[31] X. Ma *et al.*, "Achieving 17.4% Efficiency of Ternary Organic Photovoltaics with Two Well-Compatible Nonfullerene Acceptors for Minimizing Energy Loss," *Adv. Energy Mater.*, vol. 10, no. 31, p. 2001404, 2020, doi: 10.1002/aenm.202001404.

[32] M. Zhang *et al.*, "Review on smart strategies for achieving highly efficient ternary polymer solar cells," *APL Mater.*, vol. 8, no. 9, p. 090703, Sep. 2020, doi: 10.1063/5.0022887.

[33] C. McDowell, M. Abdelsamie, M. F. Toney, and G. C. Bazan, "Solvent Additives: Key Morphology-Directing Agents for Solution-Processed Organic Solar Cells", doi: 10.1002/adma.201707114.

[34] L. Zhu *et al.*, "Progress and prospects of the morphology of non-fullerene acceptor based high-efficiency organic solar cells," *Energy Environ. Sci.*, vol. 14, no. 8, pp. 4341–4357, Aug. 2021, doi: 10.1039/D1EE01220G.

[35] Q. Liang *et al.*, "Recent advances in effect of crystallization dynamics process on the morphology of active layer in organic solar cells," *Battery Energy*, vol. 3, no. 4, p. 20230073, 2024, doi: 10.1002/bte2.20230073.

[36] J. Xie *et al.*, "Synergistic Regulation of Crystallization Kinetics of Donor/Acceptor by New Volatile Additives for High Performance Organic Solar Cells," *Adv. Funct. Mater.*, Mar. 2024, doi: 10.1002/adfm.202402281.

[37] S. Mahdy, M. Feteha, M. Soliman, H. Hussien, T. Sadat-Shafai, and S. Ebrahim, "Effect of solvent and thermal annealing on D18/Y6 polymer solar cells," *J. Mater. Sci.*, vol. 58, no. 46, pp. 17543–17556, Dec. 2023, doi: 10.1007/s10853-023-09095-x.

[38] I. Babutan, O. Todor-Boer, L. I. Atanase, A. Vulpoi, S. Simon, and I. Botiz, "Self-assembly of block copolymers on surfaces exposed to space-confined solvent vapor annealing," *Polymers*, vol. 273, p. 125881, Apr. 2023, doi: 10.1016/j.polymer.2023.125881.

[39] I. Babutan, O. Todor-Boer, L. I. Atanase, A. Vulpoi, and I. Botiz, "Crystallization of Poly(ethylene oxide)-Based Triblock Copolymers in Films Swollen-Rich in Solvent Vapors," *Coatings*, vol. 13, no. 5, p. 918, May 2023, doi: 10.3390/coatings13050918.

[40] I. Babutan, O. Todor-Boer, L. I. Atanase, A. Vulpoi, and I. Botiz, "Self-Assembly of Block Copolymers in Thin Films Swollen-Rich in Solvent Vapors," *Polymers*, vol. 15, no. 8, p. 1900, Apr. 2023, doi: 10.3390/polym15081900.

[41] "Morphological Characteristics of Biopolymer Thin Films Swollen-Rich in Solvent Vapors." Accessed: Mar. 25, 2025. [Online]. Available: https://www.mdpi.com/2313-7673/9/7/396

[42] "Y6, BTP-4F | Acceptor Molecule for NFA OPVs | CAS 2304444-49-1 | Ossila." Accessed: Mar. 26, 2025. [Online]. Available: https://www.ossila.com/products/y6?_pos=1&_sid=6d065b7e5&_ss=r

[43] "Y6 in Solar Cells: Structure, Benefits, Alternatives and Donors | Ossila." Accessed: Mar. 26, 2025. [Online]. Available: https://www.ossila.com/pages/what-are-y6-acceptors?_pos=3&_sid=6d065b7e5&_ss=r

[44] J. Yuan and Y. Zou, "The history and development of Y6," *Org. Electron.*, vol. 102, p. 106436, Mar. 2022, doi: 10.1016/j.orgel.2022.106436.

[45] "BTP-4F-12, Y6-BO (Y12)," Ossila. Accessed: Mar. 26, 2025. [Online]. Available: https://www.ossila.com/products/btp-4f-12

[46] I. Botiz, N. Grozev, H. Schlaad, and G. Reiter, "The influence of protic non-solvents present in the environment on structure formation of poly(γ-benzyl-l-glutamate) in organic solvents," *Soft Matter*, vol. 4, no. 5, pp. 993–1002, 2008, doi: 10.1039/B719946E.

[47] I. Botiz *et al.*, "Convective self-assembly of π-conjugated oligomers and polymers," *J. Mater. Chem. C*, vol. 5, no. 10, pp. 2513–2518, Mar. 2017, doi: 10.1039/C7TC00063D.

[48] "What is AFM? Learn about Atomic Force Microscopy! - NanoAndMore." Accessed: May 01, 2025. [Online]. Available: https://www.nanoandmore.com/what-is-atomic-force-microscopy?gad_campaignid=1370796205&gad_source=1&gbraid=0AAAAAD-XR36cqreOPZlv71kCF2lZVhIfg&gclid=Cj0KCQjwt8zABhDKARIsAHXuD7YEHuqS7XP7xci1F06NcK6zXqjvJ8jUfOytJvuLxql7_fPwem3CusQaAjEQEALw_wcB

[49] "Atomic Force Microscopy | Nanoscience Instruments." Accessed: May 01, 2025. [Online]. Available: https://www.nanoscience.com/techniques/atomic-force-microscopy/

[50] "Spectrophotometry - an overview | ScienceDirect Topics." Accessed: May 01, 2025. [Online]. Available: https://www.sciencedirect.com/topics/physics-and-astronomy/spectrophotometry

[51] K. Rahimi, I. Botiz, J. O. Agumba, S. Motamen, N. Stingelin, and G. Reiter, "Light absorption of poly(3-hexylthiophene) single crystals," *RSC Adv.*, vol. 4, no. 22, pp. 11121–11123, Feb. 2014, doi: 10.1039/C3RA47064D.

[52] M. Zhang *et al.*, "High-Efficiency Organic Photovoltaics using Eutectic Acceptor Fibrils to Achieve Current Amplification," *Adv. Mater.*, vol. 33, no. 18, p. 2007177, 2021, doi: 10.1002/adma.202007177.

[53] G. Yao *et al.*, "Preaggregation in Solution Producing Multiple Crystal Forms of Y6 Corresponding to a Variation of Miscibility in PM6-Based Ternary Solar Cells," *ACS Appl. Energy Mater.*, vol. 5, no. 1, pp. 1193–1204, Jan. 2022, doi: 10.1021/acsaem.1c03578.